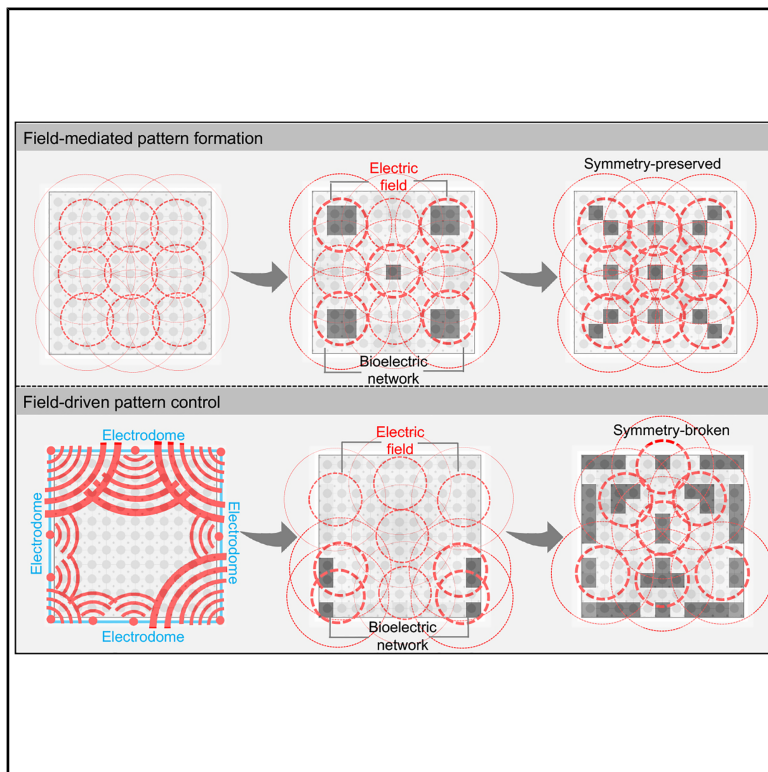


Field-mediated bioelectric basis of morphogenetic prepatternning

Graphical abstract



Authors

Santosh Manicka, Michael Levin

Correspondence

michael.levin@tufts.edu

In brief

The endogenous electric field of a simplified bioelectric network model of an embryo facilitates the autonomous formation of voltage patterns. Transient exogenous electric fields can leverage this property by acting as a steering handle to mold the pattern into desired shapes, thus offering a potentially novel non-invasive regulator of morphogenesis.

Highlights

- Intrinsic electric field enables bioelectric network patterning via negative feedback
- Pattern complexity is maximized when field is maximally causal and compressed
- Transient external fields malleably steer pattern configuration
- Patterning seed is direct or coded depending on cells' field sensitivity

Article

Field-mediated bioelectric basis of morphogenetic prepatternning

Santosh Manicka¹ and Michael Levin^{1,2,*}

¹Allen Discovery Center at Tufts University, Medford, MA 02155, USA

²Lead contact

*Correspondence: michael.levin@tufts.edu

<https://doi.org/10.1016/j.xcrp.2025.102865>

SUMMARY

Intercellular bioelectric communication plays an important role in morphogenesis, often modeled using localized non-neural networks generating spatial patterns of membrane potential (V_{mem}). Here, we find that the electrostatic field contributes to this process, via a synergetics (à la Haken)-based mechanism, by enhancing the complexity of V_{mem} patterns through a coarse-grained projection. We leverage this property of the field to automatically optimize transient signals from a symmetry-breaking organizer region in the boundary of the tissue to mold V_{mem} patterns in the bulk. Two models optimized in this way exhibit contrasting “mosaic” and “stigmergic” pattern-coding strategies, depending on their field sensitivity strengths. Interestingly, the stigmergic model recapitulates the qualitative developmental sequence of the bioelectric craniofacial prepattern observed in frog embryos. These results highlight the potential of the electric field both as a facilitator of collective patterning and as a macroscale interventional target for applications in regenerative medicine and bioengineering.

INTRODUCTION

Biological control systems, such as the ones ensuring reliable, robust embryonic and regenerative morphogenesis,^{1–4} are an important and fascinating target of inquiry. Understanding these systems has direct relevance to the regenerative medicine of birth defects, injury, and cancer as well as to the fundamental dynamics of evolutionary developmental biology. An important question that remains open in this endeavor is how these systems globally integrate information: what is required for consistent morphogenetic pattern formation to result from the activities of large numbers of cells to produce a specific anatomical outcome?^{5,6} It has been suggested that the key to this puzzle lies in the fact that biological systems are often characterized by emergent multiscale architectures,^{7–10} making them amenable to coarse-grained top-down control that generates highly coordinated, complex downstream effects.¹¹ Could emergent biophysical fields, such as the electric field, serve as such macroscopic “control knobs” to facilitate the spatiotemporal integration and regulation of developmental patterns, whether wild-type or synthetic?^{12–16} Here, we explore this idea using a computational approach that employs a field-based mechanism of patterning, serving as a proof of principle of pattern mediation and control in biological systems.

The establishment of morphogenetic patterns is regulated by a combination of several local and global factors including gene regulation,^{17–20} the influence of organizers,^{21–25} cell-cell signaling,²⁶ morphogen gradients,^{27–30} bioelectric prepatterns (spatial patterns of resting potential that precede overt phenotypic patterns),^{31–35} hormonal signaling,³⁶ and purely physical

factors such as mechanical forces and tissue geometry.^{19,37–41} For instance, segmentation patterns along the anterior-posterior axis in model organisms such as zebrafish and *Drosophila* are generated by mechanisms such as morphogen gradients together with genetically encoded expression threshold profiles³⁰ or by developmental clocks in conjunction with the sequential ordering of genes (e.g., *Hox*) that correspond to the axial identities of the segments.²⁸ These relatively simple phenomena may be sufficient for establishing simple one-dimensional positional-information maps and the corresponding morphogenetic patterns, but does the construction of more complex patterns require more complex processes? Here, we suggest that even relatively simple processes that leverage a spatially extensive field may be sufficient for not only facilitating but also manipulating the generation of complex patterns in the context of bioelectric network patterning.

One important set of biological regulators concerns ionic signaling; all cells, not just neurons, communicate electrically *in vivo*.^{42,43} Non-neural bioelectric signaling has now been implicated in embryogenesis, regeneration, and cancer suppression (reviewed elsewhere^{32,44,45}). Bioelectric properties in tissue have been shown to underlie prepatterns regulating the formation of complex structures such as the vertebrate face^{46,47}, axial patterning of the anterior-posterior,^{48,49} dorsoventral,⁵⁰ and left-right^{51,52} axes; the location and identity of specific organs such as the eye^{53,54} and the egg-ovary system^{55–59}; patterning of epithelia such as skin and feathers⁶⁰; and size control.^{61–65} Numerous gene expression⁶⁶ and epigenetic⁶⁷ targets lie downstream of changes in bioelectric state. Moreover, transduction machinery has been characterized for converting changes of

cell resting potential into second-messenger cascades that impact cell behavior such as migration, differentiation, and proliferation.^{68–70} However, bioelectricity is fundamentally not a single-cell property; it has been argued^{31,71} that its true import lies in the high-level, coarse-grained, tissue-wide information structures (prepatterns) that serve as master regulators for complex cascades of pattern formation. Indeed, modulation of resting potential via ion-channel misexpression, pharmacological modulation of channels and pumps, and optogenetics has enabled triggering of whole-organ formation,⁵³ appendage regeneration,⁷² and tumor normalization.^{67,73} In other words, spatiotemporal patterns of bioelectric state across tissues trigger complex, organ-level, downstream outcomes and all of the transcriptional changes that they require.

The bioelectric control system has been suggested not only as a promising therapeutic target for biomedicine^{74–80} but also as an important component of the machinery of evolutionary changes in body structure and behavior.^{81–83} Indeed, it is now becoming clear that modifying the bioelectric prepatterns observed in tissues can be modified to control downstream anatomy, such as repairing birth defects, in accordance with the predictions of a computational model.^{84–86} However, a fundamental capability gap is being able to induce desired bioelectric patterns. Because of the difficulty of establishing standing, long-term, spatially complex patterns of resting potential with electrodes, recent efforts have adopted a micromanagement strategy relying on computational models for picking electroceutical drugs (establishing patterns by turning channels on and off and relying on the downstream properties of the excitable medium of cells).^{77,87,88} Could including a field component in the models facilitate *macroscopic* control of downstream non-neural bioelectric events via electrode array methods, providing a new toolkit for regenerative medicine beyond the use of electrodes to target neuronal processes^{89,90}?

Although classic work in this domain used the tools of applied and measured electric fields,^{91–98} more modern approaches have almost exclusively focused on the resting potential of individual cells^{99–101} and the rules governing state transitions between neighbors and across tissue.^{102–109} In effect, this agent-based, discrete approach mirrors a key conceptual workhorse in neuroscience—dynamics of neuronal networks and the patterns of information that propagate across these discrete networked nodes according to local interaction rules. It should be noted, however, that a founding father of bioelectricity, Harold S. Burr, explicitly predicted that non-neural bioelectricity would not betray its true depth of understanding and applications until its *field* aspect was incorporated along with the traditional particle aspect (the latter is how he referred to the discrete approach). He believed that, even though the field was produced by the underlying discrete components, its activity engendered “wholeness” and “organization,” concepts that capture the macroscopic aspects of a system¹¹⁰ (in this, he anticipated, but did not have access to, recent developments of mathematical tools quantifying collective dynamics and emergent levels of causation). Despite his warning in 1935,^{110–114} very little work on incorporating actual electric fields into the quantitative modeling of endogenous developmental bioelectricity has been done. Likewise, the major approaches of targeting bioelectric controls for

biomedical applications in morphogenesis have not exploited field concepts. However, the tide is shifting in neuroscience, with field aspects of neural function starting to take center stage as mediators of memory and long-range coherence.^{115–126} Here, we explore the incorporation of true field aspects in a non-neural bioelectric model of morphogenetic pattern generation.

Could a field facilitate the global integration and control of morphogenetic patterning? To be clear, a number of purely local modalities, such as cells responding to local concentrations of diffusive long-range biochemical gradients³⁰ and local cell-cell signaling, have been proposed to generate complex patterns,^{127–130} locally detect simple global patterns,¹³¹ and adaptively scale simple patterns to system size.¹³² However, in general, models that rely on emergence of global organization from local interactions are hard to translate into intervention strategies because they imply the need to either solve a difficult inverse problem on an iterative dynamic system or to micro-manage all of the individual components toward the desired outcome at their respective positions (some examples are discussed elsewhere^{133–136}). A different type of modeling framework explicitly incorporates a field or some other long-range analog of it. Examples include neuroscientific models^{115,137–141} involving “ephaptic coupling” of neurons via endogenous electric fields, aimed at studying its effect on neuronal excitability, spike timing, synchronization, memory, etc.; cellular automata models such as Lenia¹⁴² and its variants^{143,144} involving “kernels” or “potential fields” with sizes ranging from local neighborhoods to entire tissues, aimed at generating life-like patterns; and a class of artificial neural network models known as “Gas-Nets”¹⁴⁵ that utilize a freely diffusing biochemical component (a type of gas) to modulate the neuronal interactions at long distances, originally designed for adaptive robot locomotion. There are also non-local reaction-diffusion (RD) models^{146,147} involving long-range interactions such as advection, protrusion, and competition, with applications ranging from biological pattern formation to ecological dynamics. A key question is whether the presence of such endogenous field-like mechanisms could make a system more amenable to exogenous, and potentially non-invasive, top-down control of complex patterning, enabling the guidance of the self-organization of complex patterns by sparse stimuli that result in specific system-level outcomes. To our knowledge, this has not yet been computationally explored.

To address this knowledge gap, we considered a conventional non-neural bioelectric network model possessing topographic short-range connectivity, and equipped it with a simple, fast-acting, and long-reaching and ephaptic biophysical field. We hypothesized that the field facilitates both the generation and macroscopic non-invasive control of complex patterns by virtue of its instant penetration into the tissue in a directed manner, a property we term “effusion.” This model is most closely related to the RD class of models described above, with the main difference being that it follows dynamics determined by coupled ordinary differential equations (ODEs) rather than partial differential equations (PDEs) along with an instantly effusing rather than a gradually diffusing factor, thereby offering both a simplification and a unique biophysical variation over RD models. The electric field, moreover, fits the description of “a continuous force field that regulates and is regulated by a discrete network of cells,”

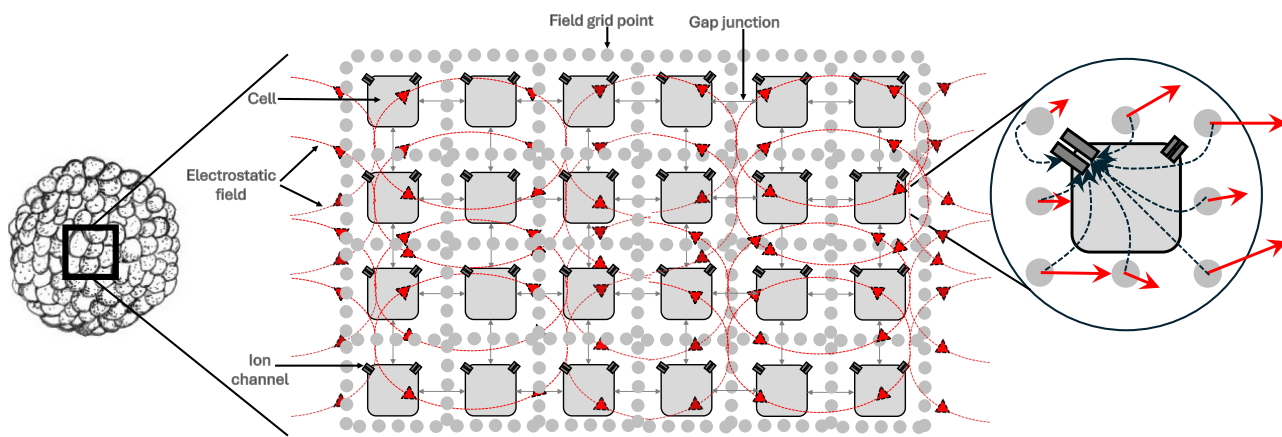


Figure 1. Schematic illustration of the model

The target of the model is a portion of an early-stage embryo such as the blastula (left), modeled as a simple 2D lattice network of bioelectric cells equipped with an electrostatic field that is collectively induced by the spatial V_{mem} configuration of the tissue (center), which in turn interacts with the V_{mem} of individual cells (right). Gray squares represent cells, with the black marks at the top corners of each cell representing a pair of generic ion channels with oppo. The thin double-headed gray arrow marks connecting neighboring cells representing gap junctions. The small filled gray circles represent the field grid points, and the red arrows passing through them and the cells represent the electrostatic field lines. The zoomed-in view of a cell on the right more clearly shows the force vectors at the field grid points (red arrows) and their modulation of the ion channel (black dashed arrows).

as had been suggested by the pioneers of the biological field concept.¹¹⁰

The aforementioned unique features of the electric field hint at its potential ability to serve as a steering handle for the self-organization of multicellular bioelectric activity patterns, a hypothesis supported by previous research showing that endogenous electric fields influence development,^{96,148,149} including phenomena such as neural crest migration,¹⁵⁰ nerve growth,¹⁵¹ and cell division orientation.¹⁵² Here, we focus on the role of the electric field in the regulation of tissue-wide bioelectric voltage patterns, both endogenously and exogenously, and concretely demonstrate it as a proof of principle using our model.

A schematic overview of the model constituting a two-dimensional sheet of cells, representing small cellular collectives, such as the ectoderm that gives rise to the vertebrate face or the brain,¹⁵³ is provided in Figure 1. Each cell in the model is equipped with a pair of generic voltage-gated ion channels, one that depolarizes the cell and the other that hyperpolarizes it. The cells are connected in the style of a plane lattice where neighboring cells are connected by voltage-gated gap junctions—electrical synapses known to play a critical role in shaping bioelectric signaling^{154–156} as well as the movement of other physiological small molecules. This core model, which has been adopted in several studies before,^{103,108,109,131,157–161} is further endowed with an electrostatic field induced by the spatial charge distribution corresponding to the membrane potentials (the potential difference across the membrane, V_{mem}) of the constituent cells, following Coulomb's laws of electrostatics.¹⁶²

This model is further equipped with a field transduction mechanism, where the average magnitude of the electrostatic forces that a cell perceives on its surface modulates its ion channel opening; that is, the ion channels are field gated besides being voltage gated. This was motivated by several “electroreception” mechanisms (the phenomenon by which an organism perceives electric fields through special electroreceptors) observed in na-

ture, ranging from atoms to entire ecosystems,^{163,164} and specific electric field transduction mechanisms employed by cells.^{120,165–174} Furthermore, a cell in our model can radiate its field through varying spatial extents (action range), but it can only perceive the field impinging on its surface (Figure 2). Overall, the model is defined by four parameters: gap junction strength (G), field transduction weight (W), field transduction threshold (B), and field action range (R), where the parameters W and B jointly characterize the field sensitivity strength. These parameters along with another central feature of the model—a negative-feedback relationship between the field and V_{mem} —determine the dynamics and the qualitative types of the inherently generated V_{mem} patterns (Figures 2 and 3). Such a relationship is necessary for pattern formation in general.^{175,176}

We use this model to ask several questions about the ways in which true field dynamics could impact bioelectrical morphogenesis via interactions with the particle (V_{mem}) components. In brief, we find that the endogenous field systematically regulates the patterning behavior of an otherwise conventional bioelectric system, as quantified by the measures of pattern complexity, dimensionality, and causal catalysis. Importantly, an optimal parameter region exists where the capacity for intrinsic patterning mediated by the endogenous field is maximized. The field achieves this by effectively emerging as a control parameter that catalyzes causal interactions among the cells, thereby driving bioelectric patterning. We then leverage this property of the field to demonstrate exogenous macroscopic pattern control in an optimal model by steering it to generate a minimal but sufficiently complex and heterogeneous V_{mem} pattern—the vertebrate face—by transiently stimulating the field around just the boundary of the tissue. Using machine-learning methods, we optimize the stimulation profiles for two different models with varying field sensitivity strengths and find that they develop disparate pattern “seeding” strategies: the weakly sensitive model adopts a direct strategy where it develops the

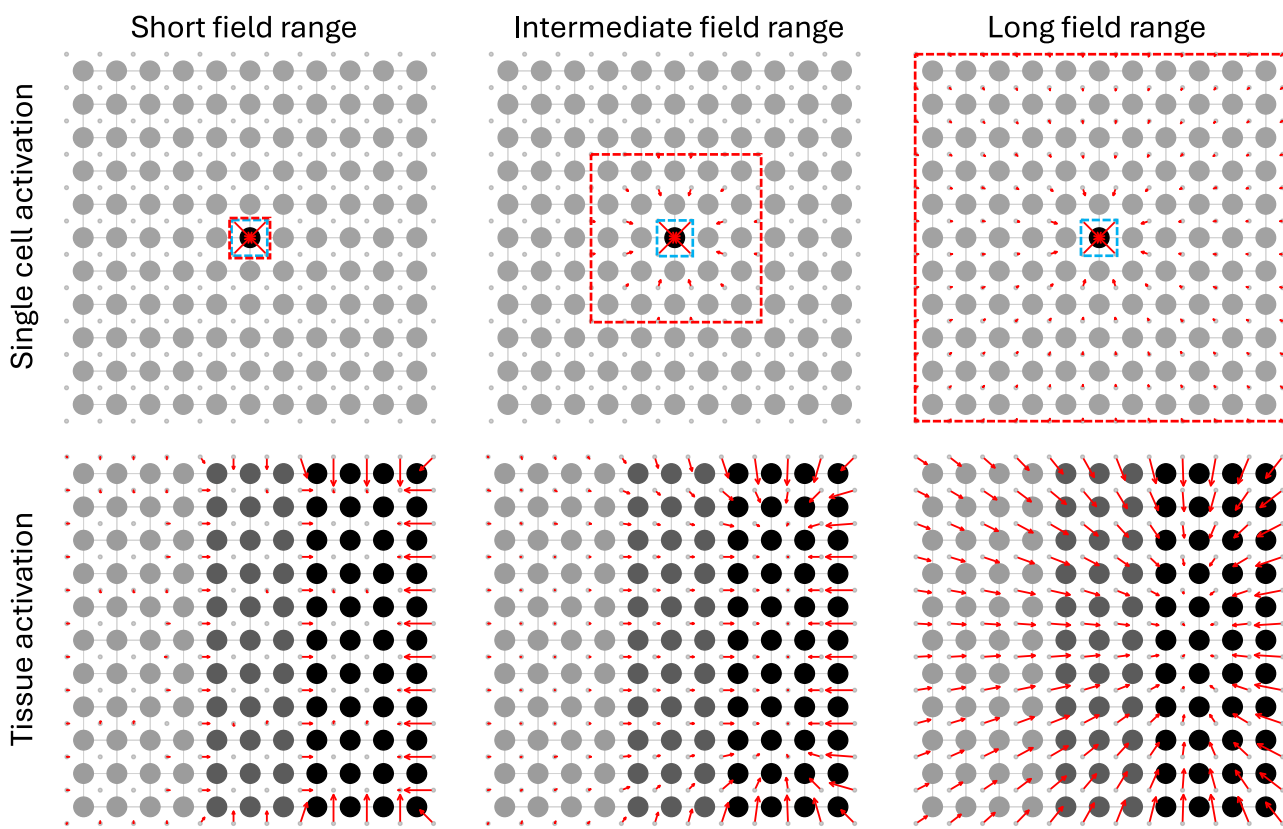


Figure 2. Variety in electrostatic force-field profiles

Different combinations of spatial V_{mem} patterns and R result in different patterns of the electrostatic force-field profiles when a single cell is bioelectrically active and all other cells have zero V_{mem} (top row) and when the entire tissue is voltage patterned (bottom row) under different extents of the field action range (columns). In the top panels, the blue dashed squares represent the field perception range and the red dashed squares represent the field action range. The red arrows in all panels represent the force vectors at the field grid points. The shades of the cells represent the voltage states, with darker shades representing more hyperpolarized potentials. When the V_{mem} of the tissue is patterned (bottom row), the pattern of the force-field profile tends to align with the V_{mem} pattern more in the case of a short field range compared to a long field range where force-field profiles do not display a banded pattern. That is, the force fields also follow a band structure similar to the banded V_{mem} pattern, where the peripheries of the band are dotted with longer vectors with the bulk containing shorter vectors.

final pattern by simply sharpening a prepattern left at the end of the stimulation; the strongly sensitive model, on the other hand, follows a more coded strategy that displays striking parallels with the actual pattern sequence observed in frog embryos.

RESULTS

Electric field enhances the complexity of V_{mem} patterns in the tissue

Embryos employ a variety of biomolecular mechanisms, such as diffusion, RD, and vector transport, as well as bioelectric prepatternning mechanisms to self-organize positional information patterns during the course of development.^{28,29,108,177–179} Could the electrostatic field give the bioelectric machinery an enhanced capacity to pattern?

To determine this, we considered the Tononi-Sporns-Edelman (TSE) complexity measure of the V_{mem} patterns.¹⁸⁰ TSE is an information-theoretic quantity that quantifies the tradeoff between integration and segregation of the V_{mem} patterns at multiple spatial scales. It is defined as the total sum of mutual information between bipartitions of the system covering all partition sizes

(details in [methods](#)). When the tissue is fully integrated, the cells tend to behave synchronously as a single whole, and, when it is fully segregated, the cells tend to behave independently—TSE is zero in both cases. Complexity is maximized when the balance between the opposing forces of integration and segregation is maximized, which is precisely what a good patterning mechanism must possess, since a pattern, by definition, requires a mixture of strongly correlated and weakly correlated regions.

We simulated an ensemble of models by sweeping its parameter space consisting of G , W , B , and R , representing the gap junction strength, field transduction weight and threshold, and field action range respectively (details in [methods](#)). For each parameter combination, we computed the TSE of the corresponding model as the average over a set of 100 V_{mem} time series each obtained from a randomly chosen initial V_{mem} configuration and run for 5,000 steps. Since TSE is typically over binary probability distributions (as inferred from time-series data) and given that the cells of our model are bistable, we computed the TSE over the binarized V_{mem} time series (details in [methods](#)).

The results ([Figure 4](#)) revealed that models with stronger field sensitivities possess higher values of TSE (80 ± 20 bits),

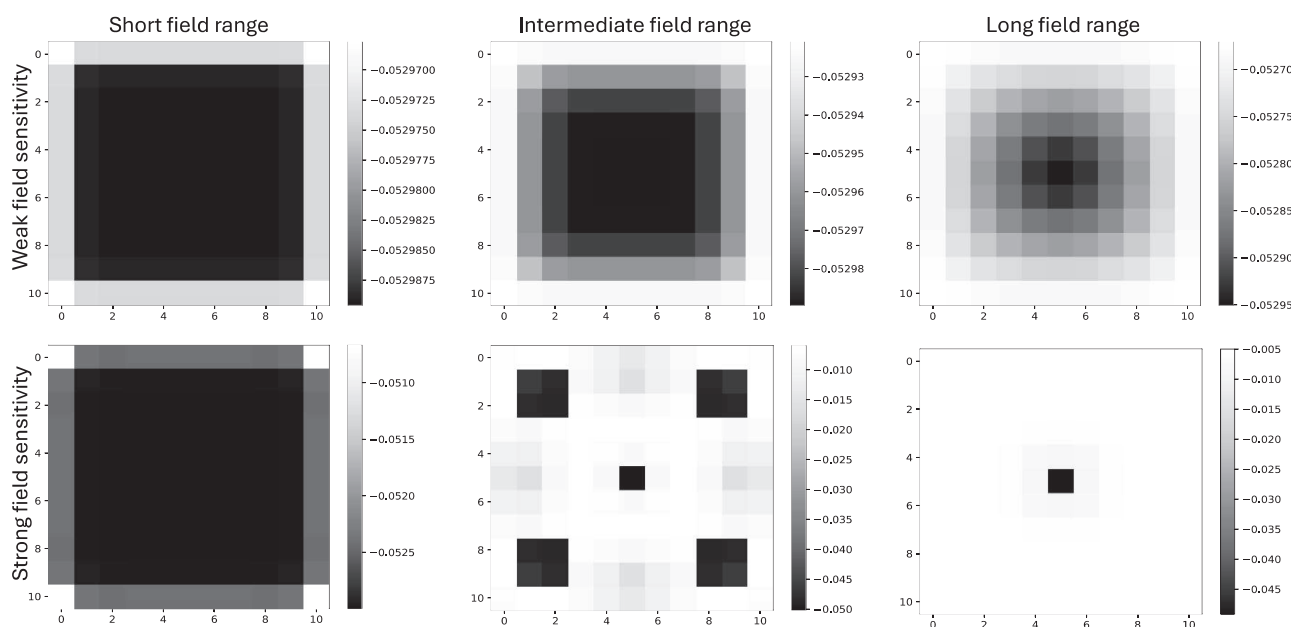


Figure 3. Variety in spatiotemporal voltage patterns

Different combinations of field sensitivity and R result in qualitatively different types of V_{mem} patterns in a 11×11 model. Top row shows models with weak field sensitivity (low W and high B), and the bottom row with strong field sensitivity (high W and low B). Columns represent models with different field action ranges, namely, short ($R = 1$), intermediate ($R = 4$), and long ranges ($R = \text{full}$). Patterns displayed are obtained after 1,000 steps of simulation each starting from homogenous initial conditions (details in [methods](#)). Shades represent voltage states, with darker shades representing more hyperpolarized potentials. Note that the most heterogeneous patterns are displayed by models with a strong field sensitivity and an intermediate field range.

whereas models with weaker field sensitivities possess lower TSE values varying in the range 0–30 bits. To put these in context, there are two types of scenario where one could expect a negligible TSE: a randomly generated pattern time series, since no correlations would be observed between partitions on average; and a version of our model that does not possess a field—it would behave like one with zero field sensitivity, in which case the entire model synchronizes to a homogenous state. Furthermore, models with stronger field sensitivities (top right region of [Figure 4](#)) possess an optimal R where TSE maximizes, the value of which depends on the corresponding parameter combination. For example, the optimal R for models with $W = 1,000$ and $B = 0.0005$ varies between short and intermediate ranges (1–4), which then expands to a range of 15–21 as B increases. These observations make sense since a higher threshold means that a cell needs to be responsive to a larger section of the tissue in order to assimilate their activities in its contribution to the complexity of the whole. Models with weaker field sensitivities (bottom left region of [Figure 4](#)) show an almost flattened TSE profile since the cells respond less to changes in the activities of neighboring cells due to the damped field-mediated communication, as a result of which the complexity is so subdued that even longer field ranges hardly make any difference.

Our results constrain the threshold electrostatic force required for complex patterning to an approximate range of 0.0005–0.005 mV/mm (estimated by the multiplying W with B and dividing by 1,000 to convert length units from meter to millimeter) which is about 100 times smaller than the theoretically expected and empirically observed value of about 0.1 mV/mm in biological

systems.^{181,182} These values can, however, be modified in our model by adjusting the relative permittivity of the cell (see model definition in [methods](#)) without changing the qualitative landscape of the results shown in [Figure 4](#). Nonetheless, the optimal field range is quite small for models generating the most complex patterns, potentially matching the limited reach of the field around the cells due to “charge-screening” effects observed in real bioelectric systems.¹⁶²

In summary, the above observations show that endowing a conventional bioelectric system with an electrostatic field enhances its patterning capacity, as shown by an increase in the complexity of the V_{mem} patterns as the ability of the cells to sense changes in the field surrounding them increases.

Electric field controls V_{mem} activity using a mechanism akin to synergetics

Electric fields play a critical role in shaping cognition and memory in the brain, as demonstrated by recent research showing that the simian brain employs them to stabilize memory formation and recall.¹¹⁵ The brain does so by leveraging the slower timescale, lower dimensionality, and higher stability of the electric field to effectively purpose it as a controller of neural activity despite their recurrent relationship.^{115–117} This is akin to a principle described by Hermann Haken in his theory of synergetics, which states that the dynamics of fast modes is constrained (Haken called it “enslaved”) by the slow modes.¹⁸³ Could viewing morphogenesis through the lens of cognition¹⁸⁴ reveal similar underlying principles of morphogenetic patterning, an idea that was also speculated elsewhere?¹⁸³ In the specific

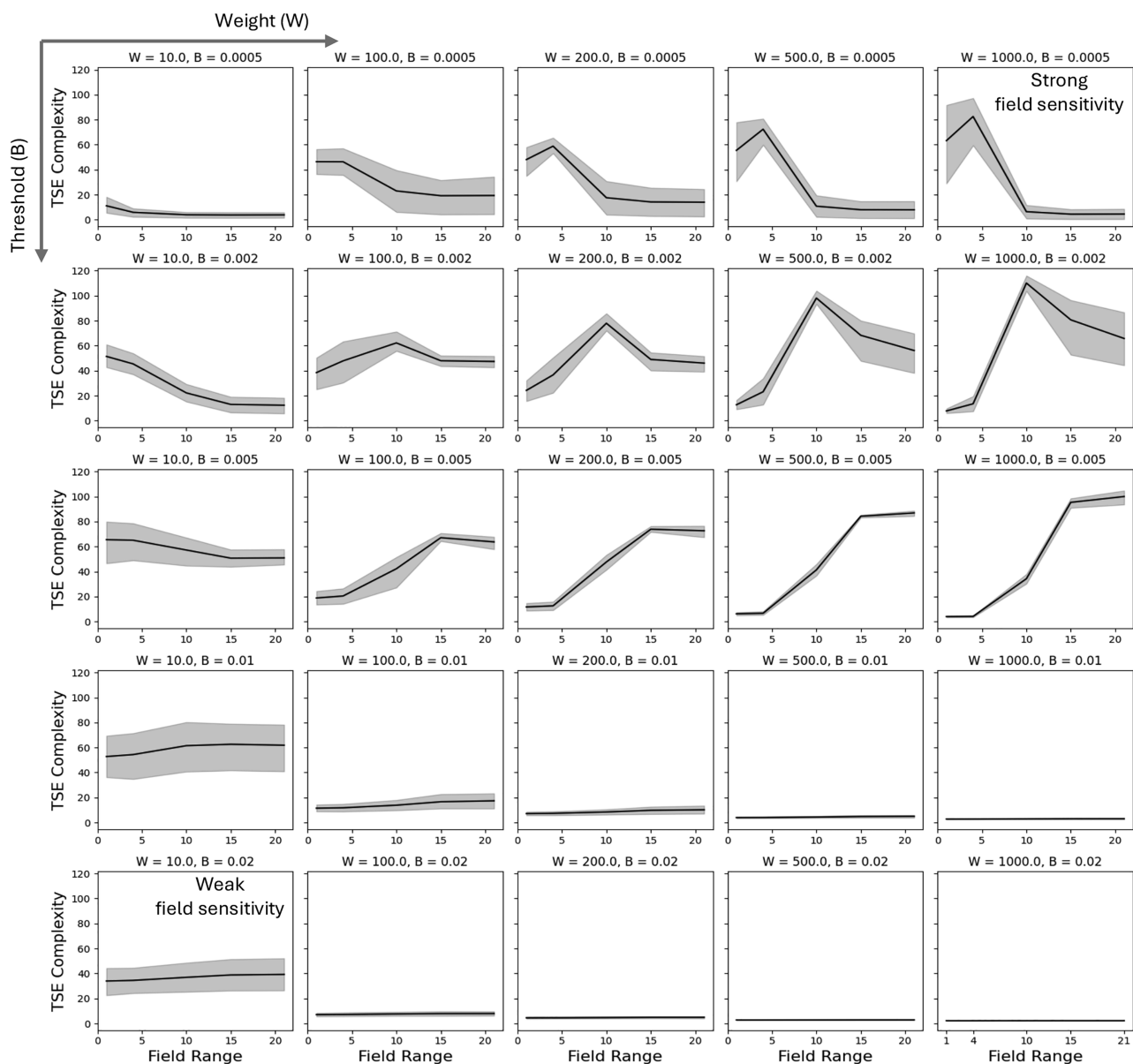


Figure 4. TSE complexity of V_{mem} patterns maximizes for models with relatively strong field sensitivities

TSE values were calculated for each parameter combination (G , R , W , and B) as the mean taken over 100 model instances each consisting of 100 randomized initial conditions simulated for 5,000 steps. Error bands represent the 95% confidence interval around the mean estimated using nonparametric bootstrapping. Variations are due to differences in G that were averaged over.

See also Figures S1–S3.

context of our model of non-neural tissue, could the electric field perform an analogous role of controlling V_{mem} activity by acting as its “guardrail” as it was originally referred to by Pinotsis and Miller¹¹⁵?

To answer this question, we considered the following measures (details in methods): (1) relative field compression (RFC), defined as the difference between the total variance explained by the first three principal component analysis (PCA) dimensions of the field and the V_{mem} time series and expressed in the dimensionless units of percentage; and (2) field influence (FI), defined

as the rate of change of V_{mem} (in units of V) with respect to small changes in the electrostatic force (V/m) between arbitrary cells and field grid points, expressed in units of distance (m), representing the displacement of the cell if the change in its electric potential energy were to be converted into kinetic energy. The first measure expresses the extent to which the field is compressed, and thus its relative temporal variability, compared to the V_{mem} pattern, while the second measure expresses the degree of control the field exerts over the V_{mem} pattern (equivalently, the amount of energy it injects into it). Together, these

measures quantify the extent to which the system displays synergistic effects à la Haken, where the field acts as a slower timescale “control parameter” and V_{mem} acts as a faster “enslaved parameter” (analogous to neural activity as described above).

As before, we constructed an ensemble of models by sweeping its parameter space consisting of G, W, B, and R (details in [methods](#)), and, for each parameter combination, we computed RFC and FI of the corresponding model as the average over a set of 100 time series each obtained from a randomly chosen initial V_{mem} configuration and run for 5,000 steps (details in [methods](#)).

We found that RFC peaked at about $35\% \pm 5\%$ for models with stronger field sensitivity and dropped to a range of -5% to 5% for models with weaker field sensitivity ([Figure 5](#)). It, moreover, stayed positive for the stronger models but sometimes became negative for the weaker models. In other words, the field not only generally tends to be more compressed than V_{mem} for the strongly sensitive models but also their difference tends to be higher compared to the weakly sensitive models. Besides, the optimal field range where RFC maximizes follows the same trend as before, in that, among the strongly sensitive models, a lower transduction threshold meant a shorter optimal field range, whereas a higher threshold meant a longer optimal field range. A higher compression of the field is also manifest in its slower variation ([Figures S1–S3](#)), meaning that strongly sensitive models display slower variations in the field compared to V_{mem} . The reason for this is that small changes in the field trigger large changes in the V_{mem} activity, but, by the time the field catches up, it steps past the threshold and the V_{mem} starts swinging in the other direction (due to negative feedback and bistability).

The qualitative trend in the behavior of FI was found to be similar to RFC across the parameter space, achieving a peak of about 3.5 ± 0.5 mm in the strongly sensitive models and dropping to 0 mm for the weakly sensitive ones. As with the above measures, FI displayed shorter optimal field ranges for the stronger models and longer ranges for the weaker models. The only exception occurred at the parameter combination of ($W = 1,000$, $B = 0.002$) where the optimal field range narrowly peaked at a value of 10 with respect to FI, whereas almost all field ranges beyond 10 were equally optimal with respect to RFC. Notwithstanding that exception, we can safely conclude that RFC and FI behave similarly in response to changes in model parameters.

These results suggest that models with stronger field sensitivity indeed display effects akin to synergetics, in that the field effectively acts as a causal control parameter of V_{mem} activity due to its slower timescale, less variability, and a stronger causal influence.

Electric field catalyzes non-local causal interactions among the cells constituting the V_{mem} pattern

Long-distance signaling plays a crucial role in morphogenesis, facilitating spatiotemporal coordination among the parts of the developing system.¹⁸⁵ Some of the major sources of long-distance communication that have so far been identified include diffusing morphogens, cellular protrusions, tunneling nanotubes, macrophage networks, as well as bioelectric signaling.^{186–188} Electric fields are also known to play a role during development in the form of cell migration (galvanotaxis), proliferation, and modulation of ion channels.^{35,165,185} Could the electric field

also facilitate direct cell-to-cell communication, especially at long distances, even if it is weak? In the context of our model, could the field catalyze the interactions among the components of the V_{mem} pattern that may not be directly connected despite being orders of magnitude weaker than V_{mem} (see [Figures S1–S3](#))?

To answer this question, we considered measures that express the degree and length of causal interactions between the cells facilitated by the field across space and time. Accordingly, we defined (1) causal strength (CS) as the absolute value of the derivative of the V_{mem} of three representative target cells of the tissue at representative time points $t > 0$ of the simulation with respect to the V_{mem} of every cell at $t = 0$, averaged over target cells and time and expressed in dimensionless units; and (2) causal distance (CD) as the distance corresponding to the highest CS, averaged over target cells and time and expressed in units of distance (m). In other words, CS quantifies the sensitivity of the V_{mem} of a cell to small changes in the V_{mem} of another cell separated in space and time, while CD indicates the distance at which the strongest CS occurs.

As before, we constructed an ensemble of models by sweeping its parameter space consisting of G, W, B, and R (details in [methods](#)), and, for each parameter combination, we computed CS and CD of the corresponding model over a single simulation trajectory initiated with homogenous conditions and run for 500 steps (details in [methods](#)).

The results ([Figure 6](#)) revealed that CS peaked at about $2 \times 10^{-3} \pm 5 \times 10^{-4}$ for models with relatively strong field sensitivity, dropping to zero for models with weaker field sensitivity. As with TSE, RFC, and FI above, CS also maximized at shorter field ranges for strongly sensitive models with a lower transduction threshold and at longer ranges for similar models but with higher thresholds—likely due to the same reasons as before. Likewise, CD maximized at about $30 \mu\text{m}$ (about three cells wide) for models with stronger field sensitivity ($B = 5 \times 10^{-4}$) with $R = 4$ (about two cells wide). It increased to $90 \mu\text{m}$ (about nine cells wide) for models with slightly weaker sensitivity ($B = 2 \times 10^{-3}$) with $R = 10$ (about 6.5 cells side). On the other hand, CD dropped to zero for models with much weaker field sensitivity.

The above results indicate that, in models with strong field sensitivity, infinitesimally small changes at the beginning of the simulation in the V_{mem} of a cell could cause changes up to 2 mV in another cell about nine cells away later in the simulation even though the action range of the cell is smaller (about 6.5 cells wide). An important implication of the above results is that CS does not necessarily decrease monotonically with distance. That is, the strongest causal influence does not necessarily stem from the closest cells—it could come from cells further away. On the other hand, the optimal CD does not have to be equal to the size of the field range; as the above observations indicate, it is typically larger but not equal to size of the tissue itself (noteworthy, since 500 steps is more than sufficient for a signal to cross the entire breadth of the tissue). Taken together, our results show that the electric field indeed has the potential to catalyze non-local causal interactions among cells in a way that is not a simple linear function of distance—a phenomenon that may be crucial for morphogenetic patterning and its control.

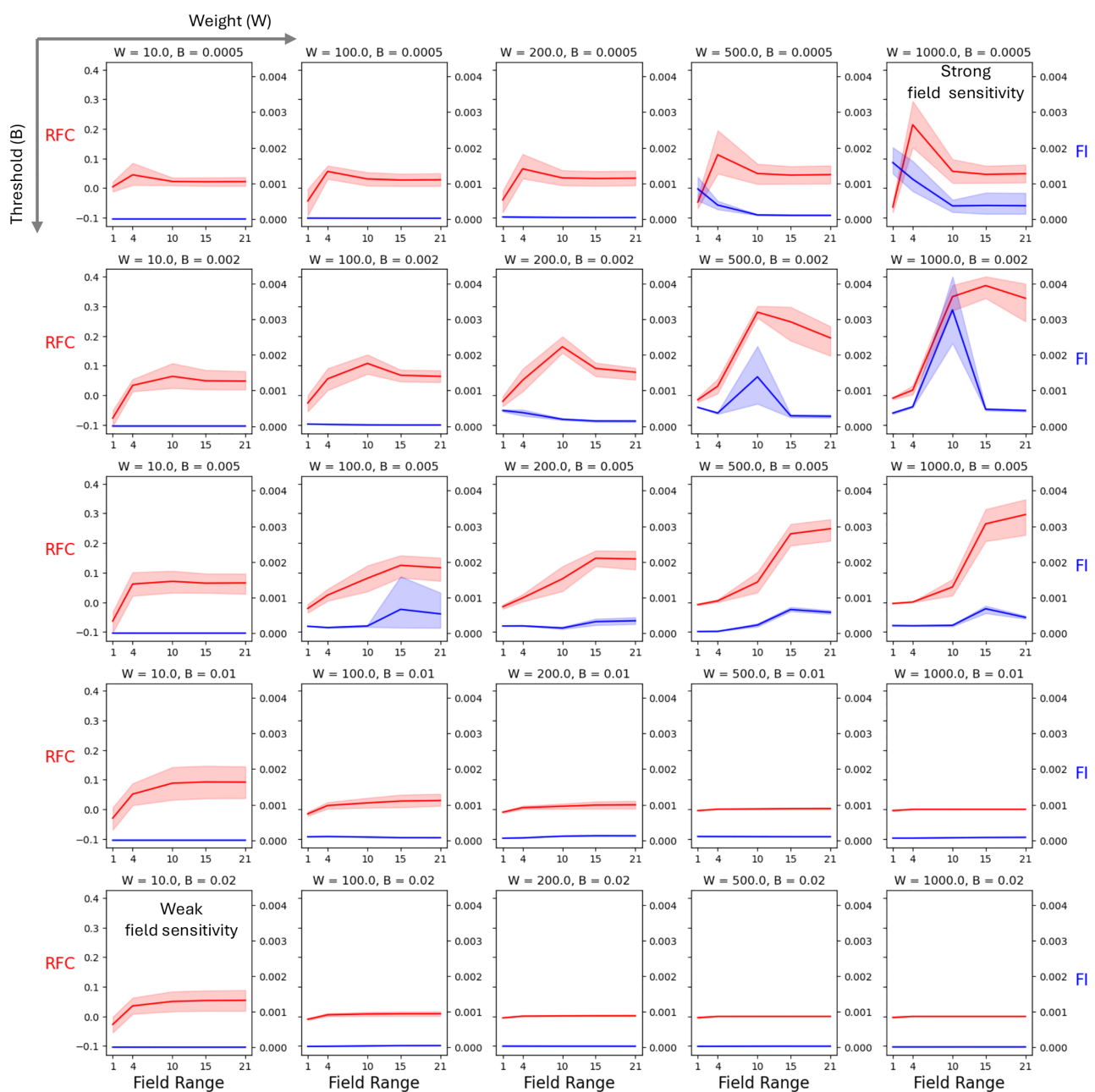


Figure 5. RFC and FI maximize for models with relatively strong field sensitivities

Red lines indicate RFC values and are plotted against the left y axis and blue is FI plotted against the right y axis. Values were calculated for each parameter combination (G , R , W , and B) as the mean taken over 100 model instances consisting of 100 randomized initial conditions simulated for 5,000 steps. Error bands represent the 95% confidence interval around the mean estimated using nonparametric bootstrapping. Variations are due to differences in G that were averaged over.

See also Figures S1–S3.

Electric field facilitates the development of a vertebrate face V_{mem} pattern in the bulk of the tissue following transient stimulation of just its boundary via mosaic- and stigmergy-based strategies

Several morphogenetic processes observed in embryos are initiated by an “organizer”—a region that supplies positional

information to distant cells.^{21,23,24} Could the electric field facilitate such patterning through transient stimulation of a small part of the tissue? Moreover, several known morphogenetic patterning processes in embryos adopt a linear and direct decoding strategy where most of the information about the pattern is supplied by the morphogens or is deduced using

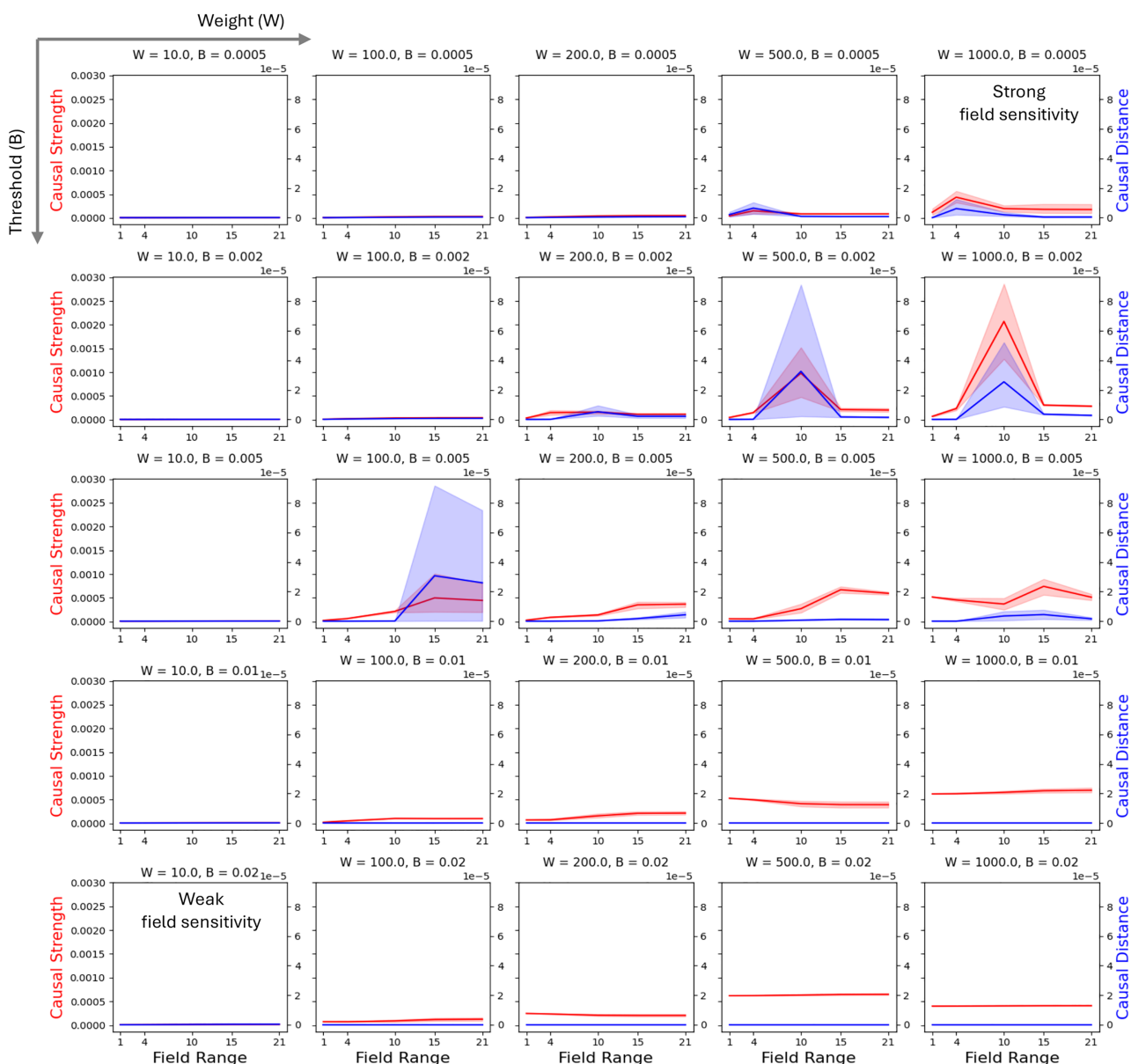


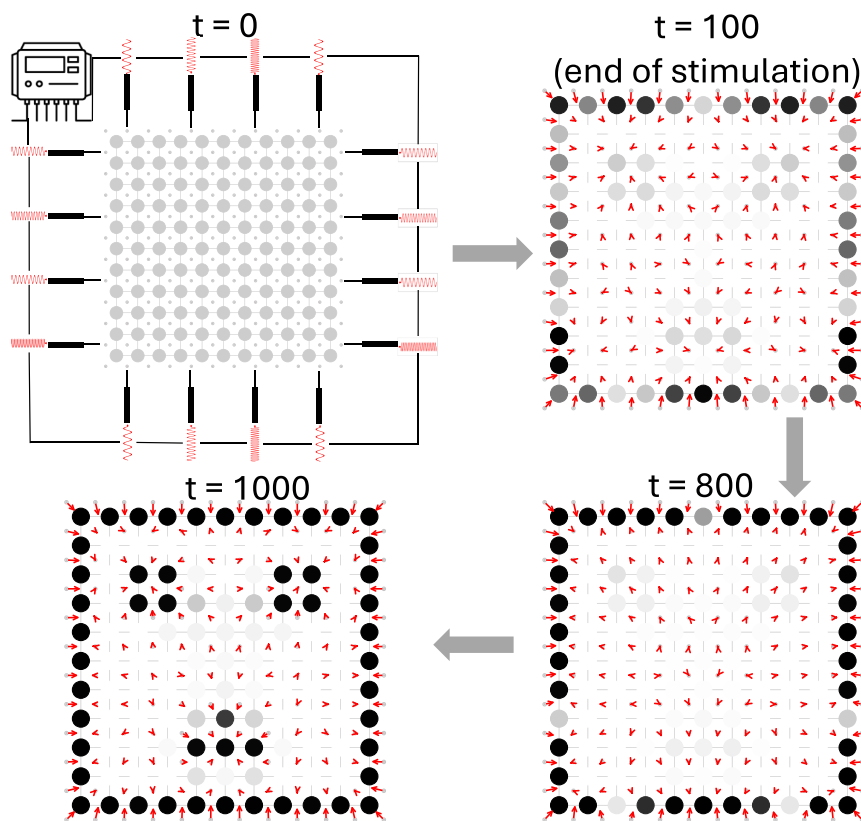
Figure 6. CS and CD maximize for models with relatively strong field sensitivities

Red lines indicate CS values and are plotted against the left y axis and blue is CD plotted against the right y axis. Values were calculated for each parameter combination (G , R , W , and B) as the mean taken over 100 model instances consisting of 100 randomized initial conditions simulated for 5,000 steps and averaged over G . Error bands represent the 95% confidence interval around the mean estimated using nonparametric bootstrapping. Variations are due to differences in G that were averaged over.

See also Figures S1–S3.

relatively simple interpretation processes such as the “French flag” and the “clock-and-wavefront” mechanisms.³⁰ Could there be more nonlinear and complex strategies where the initial information supplied by an organizer-like entity is limited and in a coded form and the system actively decodes it to generate the full pattern? To put it in concrete terms, we asked whether we could prime our model to bootstrap a full vertebral face pattern in the bulk of the tissue by stimulating only its boundary.

To explore this idea, we leveraged machine-learning techniques to optimize the signals required for generating a face-like V_{mem} pattern in the full tissue following a transient stimulation of only the field grid points located around the boundary of the tissue. For this purpose, we chose a pair of field transduction parameter sets corresponding to the strongly sensitive and weakly sensitive categories, representing the extremes of a potential range of patterning strategies that the system might employ (Figures 4, 5, and 6). Specifically, we chose the



parameter combinations ($W = 1,000$, $B = 0.0005$) corresponding to a strongly sensitive model, and ($W = 10$, $B = 0.02$) for a weakly sensitive model, with the field range set to 4 and the gap junction strength set to 0.05 in both cases. We set R to 4 since that is one of the most optimal parameters of the model that maximizes its patterning capabilities, as seen in the results above.

We adopted an oscillatory paradigm to stimulate the boundary due to its potential ability to facilitate complex patterning via wave superpositions in the bulk—an approach loosely inspired by phenomena such as cymatics (the formation of patterns in particles scattered over an elastic surface when exposed to sound waves)¹⁸⁹ and bulk-boundary correspondence of the holographic principle (an idea in physics that suggests that the information about a bulk region of space could be encoded in its lower-dimensional boundary).¹⁹⁰ Moreover, in order to capture the mechanism that organizers employ in actual embryogenic patterning, the stimulations were designed to be transient and last for only an initial fraction (100 steps) of the total simulation time (1,000 steps). We used a machine-learning algorithm called gradient descent¹⁹¹ to learn the optimal values of the pulsating inputs, namely the amplitudes and frequencies of the inputs to be applied at the field grid points situated around the boundary of the tissue with the objective of generating a face-like pattern (details in methods). When the models were optimized in this way (Figure S5), they developed very different patterning strategies (Figures 7 and 8).

The first strategy is what we call a mosaic mechanism, where, following the brief stimulation period ($t = 100$), the weakly sensi-

Figure 7. Mosaic model develops the face pattern in a linear fashion

A sequence of snapshots of the combined V_{mem} pattern and force-field profiles shows a gradual sharpening of a face-like prepattern. This model has the following fixed set of parameter values: $R = 4$, $G = 0.05$, $W = 10$, and $B = 0.02$. The only values that were optimized using machine learning were the amplitudes and frequencies of the initial transient stimulation applied at the 44 field grid points lying at the boundary of the tissue (top left). At $t = 0$, the oscillatory stimulation is applied and continued until $t = 100$. The full pattern is formed at $t = 1,000$. The profile at an intermediate time point of $t = 800$ is also shown. Lighter shades of the cells represent cells with depolarized potentials of about -5 mV, and darker shades correspond to hyperpolarized potentials of about -55 mV. Red arrows indicate force-field vectors at the field grid points.

tive tissue is left in what could be conceived as a prepattern consisting of a vague outline of a face that then sharpens into the full face pattern at $t = 1,000$ (Figure 7). The corresponding force-field profiles suggest a linear decoding strategy where each region of the pattern, namely the skin, eyes, nose, and mouth, simply increasingly hyperpo-

larize without involving any intricate mechanism of coordination. This is evident upon visual inspection when at $t = 100$ the field vectors point weakly to the features of the pattern, then, at $t = 800$, they all point to the boundary since the cells there are the first ones to hyperpolarize, and finally, at $t = 1,000$, when all the features respectively hyperpolarize, the field vectors immediately surrounding them point toward them.

The second strategy is what we call a stigmergic mechanism displayed by the strongly sensitive model (Figure 8). It is a more nonlinear strategy—evident in the pattern observed at the end of stimulation ($t = 100$) that bears no resemblance to the final face pattern; in fact, the pattern in the bulk is just a monotonic pattern that increasingly hyperpolarizes toward the center of the tissue. The nonlinearity of patterning becomes further apparent in the rest of the sequence, which involves a stigmergic communication between parts of the bulk and the boundary, resulting in a gradual “sculpting” of the face. This phenomenon is exemplified in the part of the sequence between $t = 700$ and $t = 850$. At $t = 700$, as the cells at the center of the tissue fully hyperpolarize, the boundary cells directly to their left and right also fully hyperpolarize even though the cells at the corners of the top side of the boundary were more bound to hyperpolarize (they were darker at $t = 100$, and, if they had followed a linear strategy, they would have fully hyperpolarized first at $t = 700$). As a result, the cells lying in between them have a weakened field around them due to opposing forces from either side, causing them to quickly hyperpolarize and form the eye region at $t = 850$ (note that the corner cells still have not fully

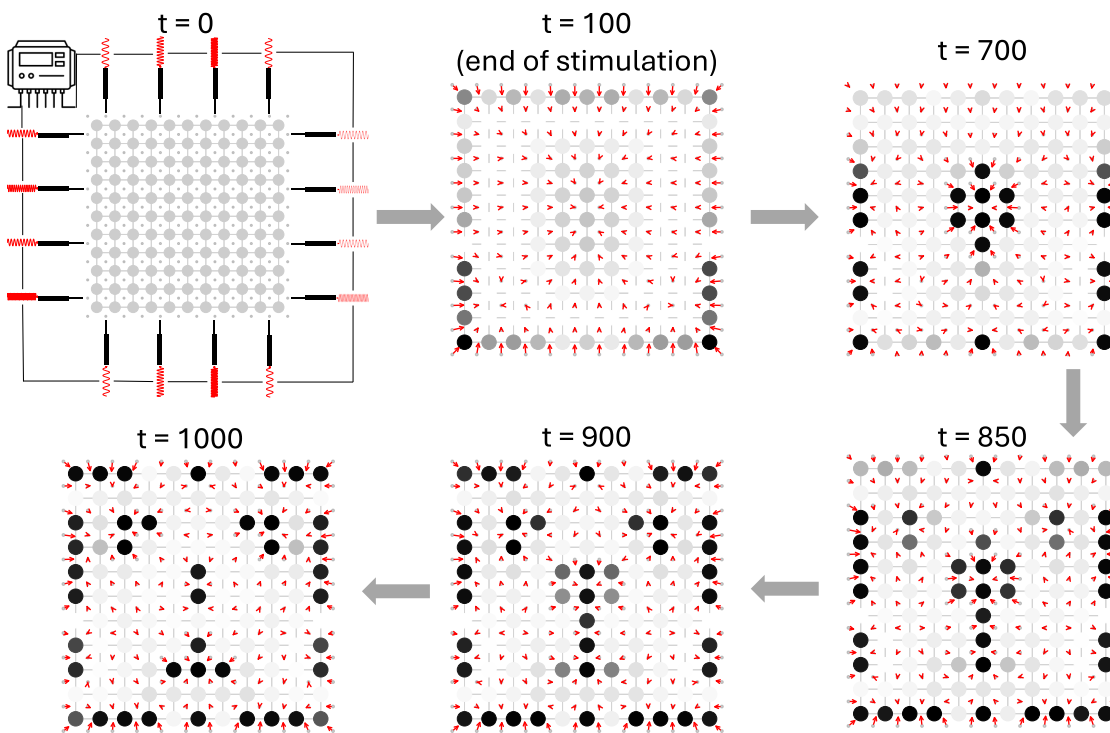


Figure 8. Stigmergic model develops the face pattern in a nonlinear fashion

A sequence of snapshots of the combined V_{mem} pattern and force-field profiles reveals a nontrivial trajectory of self-organization from an initial pattern that does not resemble a face. This model has the following fixed set of parameter values: $R = 4$, $G = 0.05$, $W = 1,000$, and $B = 0.0005$. The only values that were optimized using machine learning were the amplitudes and frequencies of the initial transient stimulation applied at the 44 field grid points lying at the boundary of the tissue (top left). At $t = 0$, the oscillatory stimulation is applied and continued until $t = 100$. The full pattern is formed at $t = 1,000$. The profile at an intermediate time point of $t = 800$ is also shown. Lighter shades represent cells with depolarized potentials of about -5 mV, and darker shades correspond to hyperpolarized potentials of about -55 mV. Red arrows indicate force-field vectors at the field grid points.

hyperpolarized). These cells further trigger other boundary cells and so on until the face is almost complete at $t = 1,000$.

To test the hypothesis that bulk-boundary communication drives the patterning in the stigmergic model but not in the mosaic model, we measured the following: (1) normalized mutual information between the bulk and the boundary (\widehat{MI}); (2) CS of interactions flowing from the boundary to the bulk (\widehat{CS}); and (3) degree of deformity in the pattern caused by the permutation of boundary states (ΔD) in both models (details in [methods](#)). We found that both \widehat{MI} and \widehat{CS} were indeed stronger in the stigmergic model, with \widehat{MI} about 3.5 times stronger and \widehat{CS} twice as strong, whereas ΔD was on average about 44.5% for the stigmergic model but 0% for the mosaic model, meaning that perturbing the boundary states resulted in significant developmental deformities in the former but not in the latter ([Table S1](#)). We also found that RFC was about thrice as strong in the stigmergic model as in the mosaic model, suggesting that the bulk-boundary interaction is not only higher but also more synergistic (à la Haken) in the former ([Table S1](#)).

It should be noted that the mosaic model required orders-of-magnitude stronger input voltages in the stimulus ([Figure S4](#)). This makes sense, since a weakly sensitive model requires stronger compensatory external inputs to supply the requisite information about the target pattern (in the form of a prepattern), as

it cannot leverage the field strongly enough to complete the pattern. A strongly sensitive model, on the other hand, only requires weak external inputs, as it can utilize the field as a scaffold to bootstrap complex patterns. This allows the model to employ mechanisms such as stigmergy that require minimal information to be supplied initially that may be sufficient to prime the nonlinearity of the system to take over and guide it in the direction of the desired outcome.

These results demonstrate that the electric field can indeed allow the model to be dynamically molded into complex patterns by priming its self-organization through transient stimulation of only the boundary of the tissue, thus circumventing the need for micromanagement that several contemporary interventional patterning methodologies entail (e.g., ion-channel modulation⁸⁶).

The stigmergic patterning model fortuitously recapitulates key qualitative features of *Xenopus* bioelectric facial prepattern development

Do the minimal vertebrate face-patterning models described above have anything to say about bioelectric prepattern development observed in real embryos? We compared patterns from various stages of our models and actual *Xenopus* embryos⁴⁷ and found that the stigmergic model indeed displayed qualitative resemblance to some of the key features of the

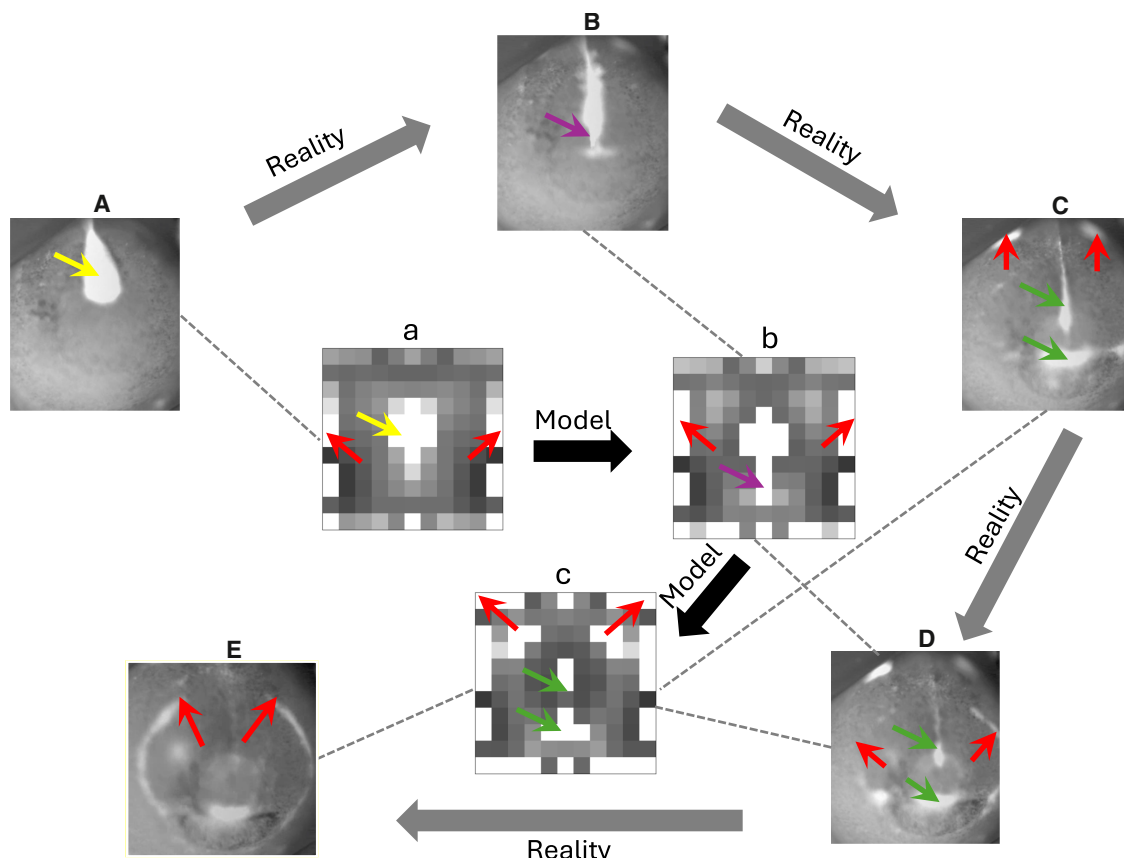


Figure 9. Stigmergic model qualitatively recapitulates the sequence of bioelectric prepattern development observed in real frog embryos

The inner sequence connected by thick black arrows represents the model and the outer sequence connected by thick gray arrows represents empirical data. Colored arrows in each image represent specific patterning events. Matching colors in model versus reality indicate matching events. The black dashed lines connecting pairs of model and empirical images indicate the existence of at least one matching event. (A)–(E) were taken from snapshots of Video S1 in Vandenberg et al.⁴⁷ and are used by permission. The electric face prepatterns shown in these panels were observed in early frog embryos by using voltage-sensitive dye technology involving CC2-DMPE and DiBAC₄ (see text for more details); lighter shades represent hyperpolarized V_{mem} states and darker shades depolarized. Although field levels were not measured in the face, these patterns represent voltage differences between regions estimated to be on the order of 20–50 mV.

developmental sequence of the craniofacial bioelectric prepattern observed in the real embryo (Figure 9).

The *Xenopus* craniofacial bioelectric prepattern development goes through several stages but we focus on the following features. The patterning sets off with a broad hyperpolarized region appearing in the anterior central portion stretching down the middle of the future face (yellow arrow in Figure 9A), later thinning out (purple arrow in Figure 9B) and splitting into features representing the future nose and the mouth (green arrows in Figure 9C). This is followed by a “ring of fire” that spreads in the form of semicircles around the left and right edges of the face (red arrows in Figure 9D), simultaneously lighting up the region of the future left eye (Figure 9E). These regionalization events are qualitatively matched by the patterning sequence displayed by the stigmergic model. Specifically, the initiation of the sequence with the formation of the broadly hyperpolarized nose region of Figure 9A is matched by a similar initiation in our model (yellow arrow in Figure 9A), with its later thinning out and splitting into two also matched by our model (purple and green arrows in Figures 9B and 9C). Furthermore, the formation of the ring of fire

with the concomitant lighting up of the eye region is also matched by our model (Figures 9B and 9C). We note, however, that the timings of these events are not matched as well as their spatial counterparts. In particular, the ring of fire and eye formation follow the nose-mouth splitting event in reality, whereas they occur in parallel in our model (red arrows appear throughout).

Notwithstanding the differences, the similarities are indeed striking and suggest the possibility that general principles of bioelectric patterning may exist in embryogenesis, especially since we did not design the model to match observed data, nor did we optimize it to develop the patterns in a specific sequence. In particular, it suggests that morphogenesis may be strongly constrained even by the relatively simple assumptions of our model.

DISCUSSION

Our goal was to understand the role of a continuous (fluid) electrostatic force field in the dynamic behavior of a discrete (solid) non-neural multicellular bioelectric network that it permeates.

Our investigations revealed that the field indeed enhances the patterning capabilities of the network, as evidenced by its ability to regulate the pattern complexity, dimensionality, and causal catalysis of the spatial V_{mem} configurations. Our results support the hypothesis that the field regulates V_{mem} patterning by effectively turning into a control parameter by virtue of its lower dimensionality and slower timescale compared to the spatial V_{mem} state, despite the circular feedback between them. This occurs in a manner consistent with the principle of synergetics, which states that fast variables are controlled by slow variables that effectively act as control parameters.¹⁸³ We leveraged these results to prime the system to develop specific target patterns simply by transiently stimulating the field surrounding the boundary of the tissue. We used machine learning, specifically automatic differentiation-based gradient descent, to optimize the oscillatory stimulus for a pair of models with opposite field sensitivity strengths to generate a vertebrate face pattern. An analysis of those models revealed that they developed the face patterns using very different strategies (namely, a mosaic- and stigmergy-based mechanism) depending on whether the field sensitivity strength was weak or strong, respectively. In summary, our work suggests that the electrostatic field could indeed function as a key facilitator of voltage patterning in embryonic tissues, thereby contributing to morphogenetic prepatternning processes in real biological systems. We interpret our results to further suggest that the electric field may have the potential to act as a top-down control knob that, when tuned appropriately, could steer a real or synthetic biological system employing bioelectricity to generate desired patterns.

The concept of biological field was originally formulated and motivated by the concept of emergence by pioneers such as Harold S. Burr, Alexander Gurwitsch, Henry Margenau, Hans Driesch, and Paul Weiss during the early twentieth century. It was originally proposed as a response to the prevailing view at the time of predeterminism or “preformism,” as explicated in Wilhelm Roux’s “mosaic theory of development,” which later became synonymous with genetic determinism.^{110,192–196} Although the field concept has been adapted in several seemingly disparate forms, we have applied its core idea, namely an integrated, continuous, fluid, and invisible (to the naked eye) entity that regulates, and is regulated by, the more segregated, discrete, rigid, and palpable constituents of a biological system.^{110,192–195} Proponents of the field concept have argued that the properties of the whole could not be deduced from the individual parts and that it is the relational organization of the system that was key. This view was supported by Hans Driesch’s groundbreaking embryo-cutting experiments,¹⁹⁴ which essentially showed that the developmental fate of the cells in an embryo should be attributed not only to their genetic states but also to their spatial locations in the tissue.¹¹⁰ Thus, the concept of positional information was born and along with it the general concept of the morphogenetic field that expressed informational and regional relationships,¹⁷⁸ the prototypical example of which is the morphogen gradient or the French-flag model, as it is popularly known.¹⁷⁷ Besides the conventional sources of positional information, such as biochemical and transcriptional gradients, patterns of bioelectric potentials can also provide such information to the cells

for appropriate differentiation during development.^{178,197} In his search for the core dynamics of substrate-invariant decision-making systems, Alan Turing proposed an early version of a biochemical basis of such a system, mimicking the self-organizing properties of embryos.^{16,130,198–203} Here, we have developed an analogous bioelectrical field basis of patterning.

We found that adding a true field dynamic to a bioelectric patterning system can enhance its capacity for emergent self-organization of morphogenetic prepatterns. Given that prepatternning and positional information are deeply connected,^{198,204} this result has implications for developmental biology, as it suggests that a bioelectric field basis of morphogenesis may indeed be viable. Our model serves as a concrete example of this broad idea that subsumes a conglomerate of related concepts and hypotheses that were originally articulated in the early twentieth century. For instance, Alexander Gurwitsch found that describing the outlines of an embryo is simpler than describing the details of its parts, a function that he proposed was carried by some kind of field.¹⁹⁴ He moreover proposed that such a field was constituted by the developing body itself that in turn was shaped and refined by the field, an idea that was shared by Harold Burr.¹⁹⁴ Our model shows that the electrostatic field could serve the role of the hypothetical field described in the early ideas, as it shares some of the requisite properties of the field stated above. For instance, if we take any of the force-field profiles shown in Figures 7 or 8 and remove all the cells, leaving only the force vectors in place, then one could see the outline of the face and not its parts. This picture would become even more coarse grained if one were to average those vectors with discrete segments of the picture. This “blurring” property of the field is also compatible with its lower dimensionality (Figure 5), as coarse graining loses (redundant) information, a property that supports Gurwitsch’s idea that it is simpler to describe outlines than the details of an embryo.

Our work goes further and shows that there may be more complex strategies for developing prepatterns compared to those exhibited by well-known mechanisms such as the French flag model,¹⁷⁷ the clock-and-wavefront model,²⁰⁵ and perhaps even the complex hierarchical patterning models.²⁰⁶ Specifically, we show that it is possible to generate complex patterns by leveraging stigmergic strategies that require neither significant incipient information such as the French flag model nor mechanisms of gradual complexification such as the hierarchical model. Moreover, our finding that the stigmergic model required stimulation at biologically plausible ranges (order of millivolts) suggests that evolution could exploit such a system for endogenous control of morphogenesis. A related phenomenon has been suggested to occur in early patterning of the left-right axis where cells on the ventral midline generate a bioelectric gradient that then impacts the axial identity of cells throughout the body by driving re-distribution of small-molecule morphogens (likely serotonin)^{52,207–209}

Our work has implications for methods leveraging macroscopic control in biological regulation. Biological regulators of morphogenesis typically exist at the microscale level: genetic manipulation is performed at the level of genes and single cells, and even bioelectric patterns are imprinted at the level of ion channels in single cells.²¹⁰ Various techniques based on a

macroscale control strategy do exist, such as placement of a single morphogen source in the embryo leading to tissue-wide patterning,²⁵ imprinting coarse-grained bioelectric prepatterns to stimulate fine-grained phenotypic expression even in arbitrary regions of the embryo,¹¹ simple transient stimulations to steer transitions between different pattern classes in RD systems,^{211,212} and stimulation of a small set of regulators to control the activity of a much larger set of components in gene-regulatory networks by leveraging redundancy, or canalization, in input-output relationships of the genes.^{213,214} While these methods can indeed be considered macroscopic in the sense that the dimensionality of control is smaller compared to that of the process being controlled, they still involve invasive interventions. Our field-based method is also macroscopic since the proportion of control points is only about 36% (44 field grid points for a total of 121 cells). However, our method is different from the aforementioned top-down approaches in that it is a non-invasive, “outside-in” intervention method that leverages the instantly effusing and non-material character of the electric field. In fact, the electrode-based stimulation of the tissue boundary could in the future be materialized in the form of an “electrodome” (analogous to the “biodome” used to stimulate frog-leg regeneration²¹⁵), a kind of active bandage^{216–218} that could be wrapped around the bioelectric tissue to be patterned.

Our work makes contributions to the hotly debated concepts of ephaptic coupling and long-distance communication without apparent long-distance connectivity. Neuronal cells have long been known to communicate not only through synaptic coupling but also via electric-field interactions known as ephaptic coupling.²¹⁹ These interactions happen without any physical connectivity (the term “ephaptic” means “touching”), and therefore they are often considered to be less pronounced compared to other conventional means.²¹⁹ However, recent research has begun to unravel the potential effects ephaptic coupling may have on a wide range of neural phenomena, such as memory, cognition, and even consciousness.^{115,116,118,120,220} This has led to proposals for including ephaptic coupling in modeling efforts, especially given the differential propagation speed it offers over synaptic and biochemical routes,²²¹ thus enabling a Turing-like setting to facilitate patterning and development.²²² Our work is most closely related to recent research that showcased the role of the electric field in establishing and maintaining memory engrams by virtue of its lower dimensionality (in the same statistical sense of variability as described above) and higher stability compared to neuronal activity.^{115–117} Our minimal model exemplifies these ideas in a non-neural setting (embryonic patterning), thereby demonstrating the potential substrate-free ability of the electric field to regulate disparate phenomena.

Electric-field-mediated ephaptic coupling has the potential to facilitate long-distance communication, which has been hypothesized, and robustly demonstrated in some cases, to play important roles in developmental phenomena such as neurulation, pigmentation, morphogenetic patterning, craniofacial development, body axis establishment, and even cancer.¹⁸⁵ Moreover, long-distance communication facilitates the diagnosis as well as treatment of injuries at a location that is spatially separated from the source.^{85,223} Our model serves as a minimal but concrete example demonstrating how long-distance communica-

tion (controlled by the field-range parameter) could facilitate morphogenetic patterning and potentially in other aspects of development. Additionally, unlike other models of long-distance communication^{85,145,224} as well as RD-based patterning models,^{135,206,225,226} our model possesses a unique “hopping” property where an activity source triggers distant parts of the tissue without setting off the cells en route (Figure 8). The bioelectric face patterning in *Xenopus* embryos indeed displays such characteristics (although it is not yet clear that they are causal), and there may be several other phenomena in development with hopping characteristics requiring field-based explanations.

Our work has certain limitations that may prohibit us from extrapolating the results to real biological systems. First, our model does not simulate the extracellular medium, which could play a role in morphogenesis by providing structural support, a medium for transmitting biochemical signals and affecting a wide range of behaviors, including cell polarity, adhesion, and migration.²²⁷ The extracellular medium may contain charged particles that may limit the penetration of the electric field into the tissue due to a phenomenon known as “charge screening.”¹⁶² Even though we partially mitigate this issue by parameterizing the reach of the field, real biological tissues may possess additional complexities that might further limit the role of the electric field in patterning processes.

As our goal was to understand the phenomenological effects of including a true field in a dynamic system, and not the physiological effects, we did not assume biophysically realistic parameters in the model. For instance, we assumed the relative permittivity of the cell as 10^7 , a value we adopted from a wide range of values reported in the literature ranging from a frequency-dependent value of 60 reported in the literature^{228–230} to static permittivity values ranging in 10^4 – 10^7 reported other studies.^{231–233} Even though the choice of this value could significantly alter the results, it is possible that it could be compensated by another unknown mechanism, thus preserving the broad character of our results. Lastly, we have not included gene-regulatory networks and a plethora of other biomolecular factors that could, in theory, weaken or strengthen the modulatory effects of the field *in vivo*.

We conclude with a brief outlook on the potential biomedical applications and future directions that our work may inspire. The regulatory role and therapeutic potential of bioelectricity during development and regeneration have been demonstrated in numerous vertebrate and invertebrate models (reviewed in Pai et al.²³⁴). The work on the *Xenopus* bioelectric face patterning, for instance, has shown that disrupting the bioelectric pattern leads to craniofacial abnormalities,⁴⁷ while introducing components of the native electric face pattern into other regions induces the formation of complex ectopic organs such as the eye.⁵³

Moreover, targeted repair of the pattern can rescue defects induced by teratogens or mutations.^{84,86,235,236} Work in frog, flatworm, and *Drosophila* models has implicated bioelectric prepatterns as instructive influences over gene expression and subsequent anatomy. Future exploitation of this interface for therapeutic purposes requires the ability to impose desired complex patterns on tissues and to understand what kinds of influences could disrupt the processes of morphogenesis in the

$$C \frac{dv_i}{dt} = -\frac{G_{p_i}(v_i - E_p)}{1 + e^{-z(v_i - v_{th})}} - \frac{G_{d_i}(v_i - E_d)}{1 + e^{-z(v_i - v_{th})}} + \sum_{j \in N_{C_i}} (v_j - v_i) G_{ij}$$

$$G_{ij} = \frac{2GG_r}{1 + \cosh(\frac{v_i - v_j}{v_0})}$$

$$G_r \frac{dG_{p_i}}{dt} = -G_{p_i} + 2W \left(\sigma \left(- \sum_{j \in N_{F_i}} \frac{\|\vec{e}_j\|}{|N_{F_i}|} + B \right) \right) - 1$$

$$\vec{e}_i = \frac{k_e}{\epsilon_r} \sum_j \frac{q_j}{\|\vec{r}_{ji}\|^2} \delta(\vec{r}_{ji} - \sqrt{rR})$$

$$q_j = Cv_j$$

Where:

$r = 5\mu m$, the radius of a cell

n_c = total number of cells

N_{C_i} = the set of neighboring cells of cell i

n_f = total number of field grid points

N_{F_i} = the set of neighboring (within perception range) field grid points of cell i

$v_i = V_{mem}$ of cell i (Volts)

\vec{e}_i = electric field vector at field grid point i ; $\|\vec{e}_i\|$ measured in (Volts/m)

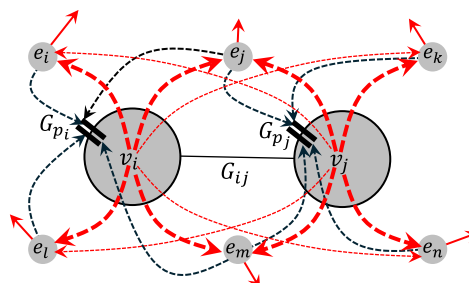
q_j = charge content of cell j (Coulombs)

\vec{r}_{ji} = distance vector from cell j to field grid point i

G_{ij} = the conductance of the gap junction connecting cells i and j (Siemens)

$G_{p_i} = P * G_r, P \in [0.0, 2.0]$

the conductance of the polarizing ion channel of cell i (Siemens)



$G_{d_i} = 1.5 nS$, the conductance of the depolarizing ion channel of cell i (S)

$G_r = 1.0e^{-9} S$, the reference value for scaling ion channel and gap junction conductance (Siemens)

$C = 0.1e^{-9} F$, the capacitance of the cell membrane (Farads)

$E_p = -55 mV$, the equilibrium potential of polarizing channel

$E_d = -5 mV$, the equilibrium potential of depolarizing channel

G = Gap junction strength $\in [0.0, 1.0]$ (A.U.)

R = field action range (A.U.)

W = field transduction weight (A.U.)

B = field transduction threshold (Volts/m)

$\sigma(\cdot)$ = sigmoid transformation

$\delta(\vec{r}_{ji} - d) = \text{delta function with value 1 when } \|\vec{r}_{ji}\| \leq d \text{ and 0 otherwise}$

$k_e = 8.987e^9 Nm^2 C^{-2}$, the Coulomb electric field constant

$\epsilon_r = 10^7$, the presumed relative permittivity of cytoplasm

Figure 10. Mathematical description of the model

An illustration of a two-cell version of the model is shown for clarity. Red arrows indicate force-field vectors at field grid points. The red dashed lines indicate the electric field lines, with their weights representing the magnitude of field strength. The black dashed lines connecting field grid points with the ion channels represent field transduction.

context of birth defects and failures to regenerate after damage. Having established several qualitative similarities with the observed real developmental sequence (Figure 9), our stigmergic model made a new prediction that disrupting the bioelectric state of the boundary *alone* could also result in craniofacial abnormalities of tissues inside it. This prediction, along with the result that the most causally influential cells may not be the spatially closest ones (Figure 6), suggests that the field may better facilitate therapeutic and biomedical interventions by providing alternatives to invasive procedures. It may also have implications for surrogate site diagnostics and interventions on deep tissues that exert their influence from a more easily accessed location. We plan to test these hypotheses in future experimental work.

Predicting downstream outcomes by intervening in upstream processes constitutes what is known as the “forward problem.”²³⁷ There is another, much harder-to-solve class of problems known as the “inverse problem,” where the goal is to find upstream states, given downstream states.^{237,238} It is known that linear encodings of morphology, such as fate maps and prepatterns, are easier to derive for given desired target morphologies due to the property called “invertibility,” something that nonlinear encodings such as gene expression patterns do not possess, making them notoriously difficult to solve.²³⁸ By leveraging machine-learning techniques, especially automatic differentiation-based gradient descent, our work offers a potential solution to the inverse problem by inferring encodings (initial conditions) in a field-based dynamic model of morphogenesis that would temporally unfold and decode into the associated

target patterns. It is noteworthy that the method underlying our approach has famously been used for the optimization of neural network inputs (not model parameters) to generate hallucinatory images in computer programs such as Google’s “deep dream.”²³⁹ In future work, we plan to exploit this technological capability to guide the patterning of real and synthetic biological systems.

Traditional electrode applications make it very difficult to induce predictable, complex patterns of stable resting potentials in non-excitable cells. However, our model suggests that, taking the field into account, it may be possible to design stimulation that results in desired bioelectric distributions in tissue. If this bears out *in vivo*, it would be a significant addition to the current toolbox of electroceuticals and wearable bioreactors^{240,241} addressing birth defects, regeneration, cancer reprogramming,^{32,77} and the bioengineering of multicellular living constructs.^{242–245}

METHODS

Model details

The bioelectric field model is a two-dimensional multicellular network of size 11×11 where the cells consist of simplified bioelectric circuits, are structurally connected via gap junctions with a topographic (lattice) connectivity, and are endowed with an electrostatic force field by virtue of having charge content that is directly determined by V_{mem} (Figure 10). The core bioelectric model, consisting of the cells equipped with a pair of generic voltage-gated polarizing and depolarizing ion channels and

voltage-gated gap-junctional intercellular connectivity was adopted from ref.^{85,158}; no extracellular medium was assumed in this model. For the model used in this paper, the conductance of the depolarizing channel, G_d , was set to a fixed value of 1.5 nanosiemens (nS) but modulated by a factor proportional to the difference between the V_{mem} of the equilibrium potential of the depolarizing channel E_d . While the conductance of the polarizing channel, G_p , was voltage gated in an analogous way, it was also subject to further modulation by the electric field in a qualitatively similar way to voltage gating (Figure 10). The joint action of the ion channels renders the cell bistable, allowing the V_{mem} to converge to one of two values, namely -5 and -55 mV separated by an unstable equilibrium at -9 mV.⁸⁵ The gap junctions were gated in such a way that it is most conductive when the V_{mem} values of the cells it connects are the same and least conductive when the difference is the greatest, allowing the tissue to achieve spatial regionalization.⁸⁵

The above core bioelectric model was further furnished with an electric field as follows. The 2D cellular lattice is enmeshed in a separate 2D “field lattice”: the cells are interspersed with “field grid points” (small gray circles in Figure 10) where the fields emitted from cells throughout the tissue aggregate (solid red arrows in Figure 10) and regulate the bioelectric state of nearby cells. Although, in reality, every conceivable point in the intercellular space would be a field grid point, we approximated it in the model as each cell being surrounded by just four grid points under the assumption that such a configuration most optimally captures the spatial relationship between the field and the cells. Thus, if the lattice dimensions of the cellular network are $r \times c$ (11×11 in our case), with the total number of cells equal to $n_c = r * c$, then the total number of field grid points would be equal to $n_f = (r + 1) * (c + 1)$. The electrostatic field in the model is established by the spatial charge distribution, where the charge content of a cell is calculated using its V_{mem} and membrane capacitance (Figure 10), following Coulomb’s laws and conventions: the magnitude of the force due to the field emitted by a cell shrinks in proportion to the inverse square of the distance from the cell, and the force vectors are pointed to the cell if it is negatively charged. The force vector at each field grid point is obtained by vector addition of the forces from all cells that contribute to it. We additionally assumed that the relative permittivity of the cytoplasm is equal to 10^7 set as per values stated in the literature.^{231–233} Even though, in principle, every cell could contribute to the net force at every field grid point, we allow the range of influence termed as the “field action range” (red boxes in Figure 2 and red dashed arrows in Figure 10) to vary as a free parameter (R) of the model. The reason is that, in real biological systems, the reach of the field is assumed to be limited due to so-called charge-screening effects.¹⁶² However, there are no data as to the actual extent of the effect, its variability across species and their developmental stages, or whether they are dynamic or stay fixed during the lifetime of the organism. Specifically, only those cells within a distance of $\sqrt{2}R$ from a field grid point can influence it. Thus, if $R = 1$, only the immediately neighboring cells influence a grid point, and, when $R = 2m - 1$, where m is the larger of the two lattice dimensions, then the whole tissue influences it. The pattern of the force-field profile

at any given point in time is thus determined by a combination of the spatial distribution of V_{mem} and R (Figure 2).

The transduction mechanism by which the electric field around a cell regulates its bioelectric state works as follows. When the average magnitude of the force vectors (black dashed arrows in Figure 10), after being transformed by a weighted (W) sigmoid, exceeds a threshold B , the G_p of the contained cell decreases, resulting in its gradual depolarization; below the threshold, G_p increases, resulting in hyperpolarization. Thus, when $B = 0$, all the cells depolarize, and when $B = \infty$ the entire tissue hyperpolarizes. For intermediate values of B , heterogeneous mixtures of states can appear, with a typical convergent pattern characterized by a set of hyperpolarized cells at the center of the tissue surrounded by depolarized cells (Figure 3). This symmetry can, however, be broken by choosing a high W , low B , and an intermediate value of R , which creates an optimal negative-feedback relationship between the field and V_{mem} (V_{mem} positively influences the field while the field negatively influences the V_{mem}), resulting in a continuous generation of novel patterns (Videos S1, S2, and S3). In general, complex patterning requires a sufficient degree of sensitivity to changes in the field that can be propagated through the tissue at varying spatiotemporal rates. The transduction parameters that determine the strength of field sensitivity are W and B . Accordingly, to better understand the effects of field sensitivity on patterning, we classify the models into two broad categories: strongly sensitive (high W and low $B > 0$) and weakly sensitive (low W and high B). The combination of field sensitivity strength and R result in qualitatively different types of V_{mem} pattern with varying degrees of complexity and heterogeneity, examples of which are shown in Figure 3.

Model simulation

The initial conditions of the variables in each simulation were set as follows: $v = -9.2$ mV and $\vec{e} = 0$ V/m for all cells; $G_d = 1.5 G_r$ for all cells; $G_p = P * G_r$ where P was randomly chosen from the range [0.0, 2.0] for each cell in simulations with heterogeneous initial conditions, and set to a constant value of 1.0 for all cells in simulations with homogenous initial conditions; $G_0 = G * G_r$; $G \in [0.0, 1.0]$ in all simulations except for the face-patterning models, where G was set to 0.05; R was varied in the range [1, 21] in all simulations except for the face-patterning models where it was set to 4; W was varied in the range [10, 1,000] in all simulations except for the face-patterning models where it was set to 10 for the mosaic model and 1,000 for the stigmergic model; and B was varied in the range [0.0005, 0.02] in all simulations except for the face-patterning models where it was set to 0.02 for the mosaic model and 0.0005 for the stigmergic model. The model equations were integrated using the standard Euler method with a fixed step size of 0.01 for about T steps where T was varied between 500 and 5,000 depending on the experiment.

Model analysis measures

The TSE measure of complexity is a measure of the balance between integration and segregation contained in a dynamic system. It is defined as the sum of mutual information between all

possible subsets of a system and their respective complements (bipartitions) of a system,¹⁸⁰ mathematically expressed as

$$TSE(X) = \sum_{k=1}^{n/2} \langle MI(X_j^k; X - X_j^k) \rangle.$$

It is equivalently stated as

$$TSE(X) = \sum_{k=1}^{n/2} \left[\langle H(X_j^k) \rangle - (k/n)H(X) \right].$$

Here, X refers to the system containing n elements, and X_j^k refers to the j^{th} subset of size k . The operator $\langle \cdot \rangle$ refers to the average taken over all possible $n!/(k!(n-k)!)$ combinations of subsets containing k elements. The terms $MI(\cdot)$ and $H(\cdot)$ refer to mutual information and Shannon entropy, respectively.²⁴⁶ TSE becomes zero in fully segregated systems where the joint entropy of the system $H(X)$ is equal to the sum of the entropies of its elements and in fully integrated systems where the joint entropies of subsets are simply scaled versions of the whole. Here, we considered random samples of subsets due to the exponentially large number of combinations of partitions for a system containing 121 elements (cells). Specifically, we considered 50 equally spaced partition sizes in the range [2, 120], and for each partition size we considered 100 randomly sampled subsets. We used the Python package dit (short for discrete information theory²⁴⁷) for computing MI and H . Since they are designed for binary data, we binarized all of the V_{mem} time series generated by our model by assigning a value of 0 to V_{mem} in the range [-40 mV, 0 mV] and 1 to V_{mem} values in the range [-80 mV, -40 mV]. We chose these ranges by observing that the V_{mem} values generated by our simulations typically varied within the range [-80 mV, 0 mV]. Moreover, the cells in our model display bistability (a tendency to assume values close to one of two equilibrium values), and therefore it made sense to binarize their states and treat them as multivariate bit vectors representing configurations of hyperpolarized and depolarized potentials.

RFC is a measure of the ratio of the dimensionality of the field to the dimensionality of V_{mem} of the tissue. We defined the dimensionality of a variable as the total variance explained by its first three PCA dimensions. Specifically, if we denote the percentage variance explained by the first three PCA dimensions of the V_{mem} time series as p_1^v , p_2^v , and p_3^v , and the corresponding terms of the field as p_1^e , p_2^e , and p_3^e (to ensure fair comparison, we computed the average magnitude of the field vectors around each cell, resulting in the same number of field variables as V_{mem} at each time point), then RFC is defined as

$$RFC = (p_1^e + p_2^e + p_3^e) - (p_1^v + p_2^v + p_3^v).$$

FI is a measure of the sensitivity of V_{mem} to the field, defined as the mean rate of change of V_{mem} of a target cell at every step of the simulation with respect to small changes in the electrostatic force of source field grid points at the beginning of the simulation averaged over all source-target combinations and time:

$$FI = \frac{\sum_{\tau=1}^T \sum_{j=1}^{n_f} \sum_{i=1}^{n_c} \left| \frac{\partial V_i(t=\tau)}{\partial e_j(t=0)} \right|}{T * n_c * n_f}.$$

CS is a measure of the strength of interaction among the cells that we first introduced in an earlier study.¹²⁹ It is defined as the mean rate of change of V_{mem} of target cells at every step of the simulation with respect to small changes in the V_{mem} of source cells at the beginning of the simulation averaged over all source-target combinations and time:

$$CS = \frac{\sum_{i=1}^{n_c} CS(i)}{n_c},$$

where

$$CS(i) = \frac{\sum_{j=1}^{n_c} CS(i,j)}{n_c},$$

where

$$CS(i,j) = \frac{\sum_{\tau=1}^T CS(i,j,\tau)}{T},$$

where

$$CS(i,j,\tau) = \left| \frac{\partial V_i(t=\tau)}{\partial V_j(t=0)} \right|.$$

CD is a measure of the distance of the most causally influential variables in a system, defined as the mean distance of a cell from five of its most causally influential cells (highest CS values), averaged over all cells:

$$CD = \frac{\sum_{i=1}^{n_c} CD(i)}{n_c},$$

where

$$CD(i) = \frac{\sum_{j \in \text{top 5 } \{CS(i,j)\}} d(i,j)}{n_c},$$

where $d(i,j)$ represents the Euclidean distance between cells i and j .

For Figures 4, 5, and 6, we estimated FI, CS, and CD rather than compute them exactly for practical reasons by choosing 50 equally spaced points in the range [1, T] and by choosing three representative target cells with locations (0,0), (0,6), and (6,6) in the 11×11 lattice, representing the cells at the corner, middle of the boundary, and center of the tissue, respectively, thereby spanning the extremities of the tissue's topography.

The normalized mutual information between the bulk and the boundary, $\widehat{MI}(Bo; Bu)$, is a measure of the proportion of correlation between the bulk and the boundary with respect to the expected correlation between partitions of similar sizes. It is defined as the ratio of MI between the bulk and the boundary

and the expected MI between any bipartition of the system where one partition is the same as the boundary and its complement naturally the size of the bulk:

$$\widehat{MI}(Bo; Bu) = \frac{MI(Bo; Bu)}{\langle MI(X_j^{[Bo]}; X - X_j^{[Bo]}) \rangle}.$$

Here, the set of indices corresponding to the bulk is denoted as $\{Bu\}$, the set of indices corresponding to the boundary $\{Bo\}$, the set of indices corresponding to a partition the size of the boundary as $\{X_j^{[Bo]}\}$, and its complement as $\{X - X_j^{[Bo]}\}$, with j referring to the index of a single partition. To estimate $\widehat{MI}(Bo; Bu)$, we randomly sampled 100 bipartitions from a possible $n!/(|Bo|!(n - |Bo|)!)$ number of bipartitions.

The normalized CS between the boundary and the bulk, $\widehat{CS}(Bu, Bo)$, is a measure of the proportion of the CS between the boundary and the bulk with respect to the expected CSs between partitions of similar sizes at a given instant of time, averaged over all time points. The notations follow the same conventions as above. As before, we estimated $\widehat{CS}(Bu, Bo)$ by randomly sampling 100 bipartitions from a possible $n!/(|Bo|!(n - |Bo|)!)$ number of bipartitions as well as by sampling τ by choosing 50 equally spaced points in the range [1, T]:

$$\widehat{CS}(Bu, Bo) = \frac{\sum_{\tau=1}^T \left(\sum_{i \in \{Bu\}} \sum_{j \in \{Bo\}} CS(i, j, \tau) \right)}{\left(\sum_{i \in \{X - X_j^{[Bo]}\}} \sum_{j \in \{X_j^{[Bo]}\}} CS(i, j, \tau) \right)}.$$

Finally, ΔD is a measure of deformity in the output pattern caused by differences in the past boundary states. Specifically, let D be the Euclidean distance between the observed pattern at the end of 1,000 simulation steps and the target vertebrate face pattern. Let D' be the Euclidean distance between the observed pattern at the end of 1,000 simulation steps following a transient perturbation and the target vertebrate face pattern. The perturbation was at the end of the stimulation period (first 100 steps), when the G_p values of the cells at the boundary of the tissue (40 cells in the 11×11 lattice) were randomly permuted. To compute the variation of the measure, we ran a set of 100 simulations each consisting of a unique permutation of the boundary states.

Optimization of external stimulus to develop target face pattern

We used machine-learning techniques to optimize the oscillatory stimulation values of the model required for generating a vertebrate face pattern (the model parameters were fixed). The stimulation was applied on a set of 44 field grid points located on the boundary of the tissue (Figures 7 and 8). However, since the target is bilaterally symmetrical (about the vertical bisection axis), the stimulation values of only 22 points had to be learned, with the other being a mirror reflection of the former. The stimulation values associated with each of those points consisted of the amplitude, phase, and frequency of the corresponding oscillatory voltage inputs; these inputs could presumably take the

form of direct currents (with respect to a fixed neutral point representing the ground), but our model does not make any explicit assumptions about it. The initial ranges associated with the variables set at the beginning of the optimization were as follows: [100 mV, 500 mV] for the absolute values of the amplitudes, [0, 2π] for the phases, and [100 Hz, 1,000 Hz] for the frequency. The learned values of the amplitudes and frequencies were allowed to step out of those initial ranges, but the phase was limited to the initial range. The stimulation period was set to the first 10% of the duration of simulation during which the stimulated points were clamped with the corresponding input voltage trains and the resulting force-field vectors were computed at all the other field grid points. We treated the stimulated field grid points as cells, meaning their charges were computed using the applied voltage and the membrane capacitance of a cell. To probe the potential variety in patterning strategies, we chose two classes of models, one with strong field sensitivity and the other with weak sensitivity. In each class, we considered a set of 100 models each with randomly initialized stimulation configuration and optimized them over 1,000 training iterations (Figure S5). We then picked the best model in each class (the mosaic and stigmergic models) for further analysis. As for the specifics of the machine-learning algorithm, we used gradient descent, a method that updates the parameters to be learned by taking a small step in the direction of the steepest descent where the height of the parameter landscape represents performance (deeper points are better).¹⁹¹ Here, we used a specific form of gradient descent method known as “resilient back-propagation,”²⁴⁸ which relies only on the sign (not the magnitude) of the gradients for updating the parameters at every iteration. For the cost function (performance), we used the root-mean-squared distance between the observed patterns during the last 10% of the simulation and the target face pattern. We used off-the-shelf implementations of these algorithms made readily available in Pytorch.²⁴⁹

RESOURCE AVAILABILITY

Lead contact

Requests for further information and resources should be directed to and will be fulfilled by the lead contact, Michael Levin (michael.levin@tufts.edu).

Materials availability

This study did not generate new materials.

Data and code availability

- All code and data used in this study are made publicly available at github.com/santamanicka/ElectricMorphogenesis with <https://doi.org/10.5281/zenodo.17164483>.
- Any additional information needed to reanalyze the data in the paper will be addressed by the [lead contact](#) upon reasonable request.

ACKNOWLEDGMENTS

We thank Patrick McMillen for helpful comments on the manuscript and Benedit Hartl for helpful feedback on the modeling approach. We thank Julia Poirier for editorial assistance with the manuscript. We gratefully acknowledge funding from the Emerald Gate Foundation.

AUTHOR CONTRIBUTIONS

M.L. and S.M. conceptualized the work. S.M. wrote code and conducted the computational experiments. M.L. and S.M. analyzed and interpreted the data and wrote the manuscript.

DECLARATION OF INTERESTS

We have filed an invention disclosure with Tufts, which may or may not be pursued toward a patent by Emerald Gate.

SUPPLEMENTAL INFORMATION

Supplemental information can be found online at <https://doi.org/10.1016/j.xcrp.2025.102865>.

Received: February 5, 2025

Revised: June 28, 2025

Accepted: September 3, 2025

REFERENCES

1. Birnbaum, K.D., and Sánchez Alvarado, A. (2008). Slicing across kingdoms: regeneration in plants and animals. *Cell* **132**, 697–710.
2. Harris, A.K. (2018). The need for a concept of shape homeostasis. *BioSystems* **173**, 65–72. <https://doi.org/10.1016/j.biosystems.2018.09.012>.
3. Levin, M. (2011). The wisdom of the body: future techniques and approaches to morphogenetic fields in regenerative medicine, developmental biology and cancer. *Regen. Med.* **6**, 667–673. <https://doi.org/10.2217/rme.11.69>.
4. Ingber, D.E., and Levin, M. (2007). What lies at the interface of regenerative medicine and developmental biology? *Development* **134**, 2541–2547. <https://doi.org/10.1242/dev.003707>.
5. Lecuit, T., and Mahadevan, L. (2017). Morphogenesis one century after *On Growth and Form*. *Development* **144**, 4197–4198.
6. Hamant, O., and Saunders, T.E. (2020). Shaping organs: shared structural principles across kingdoms. *Annu. Rev. Cell Dev. Biol.* **36**, 385–410.
7. Je'reme Feret, V.D., Jean, K., Harmer, R., and Fontana, W. (2009). Internal coarse-graining of molecular systems. *Proc. Natl. Acad. Sci. USA* **106**, 6453–6458.
8. Kim, H., Valentini, G., Hanson, J., and Walker, S.I. (2021). Informational architecture across non-living and living collectives. *Theory Biosci.* **140**, 325–341. <https://doi.org/10.1007/s12064-020-00331-5>.
9. Klein, B., and Hoel, E. (2020). The Emergence of Informative Higher Scales in Complex Networks. *Complexity* **2020**, 1–12. <https://doi.org/10.1155/2020/893256>.
10. Levin, M. (2023). Darwin's agential materials: evolutionary implications of multiscale competency in developmental biology. *Cell. Mol. Life Sci.* **80**, 142. <https://doi.org/10.1007/s00018-023-04790-z>.
11. Pezzulo, G., and Levin, M. (2016). Top-down models in biology: explanation and control of complex living systems above the molecular level. *J. R. Soc. Interface* **13**, 20160555. <https://doi.org/10.1098/rsif.2016.0555>.
12. Goodwin, B.C., and Trainor, L.E. (1980). A field description of the cleavage process in embryogenesis. *J. Theor. Biol.* **85**, 757–770.
13. French, V., Bryant, P.J., and Bryant, S.V. (1976). Pattern regulation in epimorphic fields. *Science* **193**, 969–981.
14. Brandts, W.A.M., and Trainor, L.E.H. (1990). A Nonlinear Field Model of Pattern-Formation - Application to Intracellular Pattern Reversal in Tetrahydrona. *J. Theor. Biol.* **146**, 57–85.
15. Brandts, W.A.M., and Trainor, L.E.H. (1990). A Nonlinear Field Model of Pattern-Formation - Intercalation in Morphalactic Regulation. *J. Theor. Biol.* **146**, 37–56.
16. Schiffmann, Y. (2005). Induction and the Turing-Child field in development. *Prog. Biophys. Mol. Biol.* **89**, 36–92. <https://doi.org/10.1016/j.pbiomolbio.2004.08.018>.
17. Spitz, F., and Furlong, E.E.M. (2012). Transcription factors: from enhancer binding to developmental control. *Nat. Rev. Genet.* **13**, 613–626.
18. Bernadskaya, Y., and Christiaen, L. (2016). Transcriptional control of developmental cell behaviors. *Annu. Rev. Cell Dev. Biol.* **32**, 77–101.
19. Smith, S.J., Rebeiz, M., and Davidson, L. (2018). From pattern to process: studies at the interface of gene regulatory networks, morphogenesis, and evolution. *Curr. Opin. Genet. Dev.* **51**, 103–110.
20. Sivakumar, A., and Kurpios, N.A. (2018). Transcriptional regulation of cell shape during organ morphogenesis. *J. Cell Biol.* **217**, 2987–3005.
21. Harland, R., and Gerhart, J. (1997). Formation and function of Spemann's organizer. *Annu. Rev. Cell Dev. Biol.* **13**, 611–667.
22. Martinez Arias, A., and Stevenson, B. (2018). On the nature and function of organizers. *Development* **145**, dev159525. <https://doi.org/10.1242/dev.159525>.
23. Bouwmeester, T. (2001). The Spemann-Mangold organizer: the control of fate specification and morphogenetic rearrangements during gastrulation in Xenopus. *Int. J. Dev. Biol.* **45**, 251–258.
24. De Robertis, E.M. (2009). Spemann's organizer and the self-regulation of embryonic fields. *Mech. Dev.* **126**, 925–941. <https://doi.org/10.1016/j.mod.2009.08.004>.
25. Houchmandzadeh, B., Wieschaus, E., and Leibler, S. (2002). Establishment of developmental precision and proportions in the early Drosophila embryo. *Nature* **415**, 798–802.
26. Eckert, J.J., Velazquez, M.A., and Fleming, T.P. (2015). Cell signalling during blastocyst morphogenesis. *Adv. Exp. Med. Biol.* **843**, 1–21.
27. Briscoe, J. (2019). Understanding Pattern Formation in Embryos: Experiment, Theory, and Simulation. *J. Comput. Biol.* **26**, 696–702. <https://doi.org/10.1089/cmb.2019.0090>.
28. Tkacik, G., and Gregor, T. (2021). The many bits of positional information. *Development* **148**, dev176065. <https://doi.org/10.1242/dev.176065>.
29. Simsek, M.F., and Özbudak, E.M. (2022). Patterning principles of morphogen gradients. *Open Biol.* **12**, 220224. <https://doi.org/10.1098/rsob.220224>.
30. Wolpert, L. (2016). Positional Information and Pattern Formation. *Curr. Top. Dev. Biol.* **117**, 597–608. <https://doi.org/10.1016/bs.ctdb.2015.11.008>.
31. Levin, M., and Martyniuk, C.J. (2018). The bioelectric code: An ancient computational medium for dynamic control of growth and form. *BioSystems* **164**, 76–93. <https://doi.org/10.1016/j.biosystems.2017.08.009>.
32. Levin, M. (2021). Bioelectric signaling: Reprogrammable circuits underlying embryogenesis, regeneration, and cancer. *Cell* **184**, 1971–1989. <https://doi.org/10.1016/j.cell.2021.02.034>.
33. Pietak, A., and Levin, M. (2018). Bioelectrical control of positional information in development and regeneration: A review of conceptual and computational advances. *Prog. Biophys. Mol. Biol.* **137**, 52–68. <https://doi.org/10.1016/j.pbiomolbio.2018.03.008>.
34. Whitehead, J.L., and Levin, M. (2019). Bioelectrical controls of morphogenesis: from ancient mechanisms of cell coordination to biomedical opportunities. *Curr. Opin. Genet. Dev.* **57**, 61–69. <https://doi.org/10.1016/j.gde.2019.06.014>.
35. Levin, M., Pezzulo, G., and Finkelstein, J.M. (2017). Endogenous Bioelectric Signaling Networks: Exploiting Voltage Gradients for Control of Growth and Form. *Annu. Rev. Biomed. Eng.* **19**, 353–387. <https://doi.org/10.1146/annurev-bioeng-071114-040647>.
36. Oliveira, A.C., Rebelo, A.R., and Homem, C.C.F. (2021). Integrating animal development: How hormones and metabolism regulate developmental transitions and brain formation. *Dev. Biol.* **475**, 256–264.

37. Nelson, C.M. (2009). Geometric control of tissue morphogenesis. *Biochim. Biophys. Acta* **1793**, 903–910. <https://doi.org/10.1016/j.bbamcr.2008.12.014>.
38. Delile, J., Herrmann, M., Peyriéras, N., and Doursat, R. (2017). A cell-based computational model of early embryogenesis coupling mechanical behaviour and gene regulation. *Nat. Commun.* **8**, 13929. <https://doi.org/10.1038/ncomms13929>.
39. Davidson, L.A., Joshi, S.D., Kim, H.Y., von Dassow, M., Zhang, L., and Zhou, J. (2010). Emergent morphogenesis: elastic mechanics of a self-deforming tissue. *J. Biomech.* **43**, 63–70. <https://doi.org/10.1016/j.jbiomech.2009.09.010>.
40. Heisenberg, C.P., and Bellaïche, Y. (2013). Forces in tissue morphogenesis and patterning. *Cell* **153**, 948–962. <https://doi.org/10.1016/j.cell.2013.05.008>.
41. Caldarelli, P., Chamolly, A., Villedieu, A., Alegria-Prévot, O., Phan, C., Gros, J., and Corson, F. (2024). Self-organized tissue mechanics underlie embryonic regulation. *Nature* **633**, 887–894.
42. Funk, R.H.W., and Scholkemann, F. (2023). The significance of bioelectricity on all levels of organization of an organism. Part 1: From the subcellular level to cells. *Prog. Biophys. Mol. Biol.* **177**, 185–201. <https://doi.org/10.1016/j.pbiomolbio.2022.12.002>.
43. Funk, R. (2013). Ion Gradients in Tissue and Organ Biology. *Biol. Syst.* **2**. <https://doi.org/10.4172/bso.1000105>.
44. Bates, E. (2015). Ion Channels in Development and Cancer. *Annu. Rev. Cell Dev. Biol.* **31**, 231–247. <https://doi.org/10.1146/annurev-cellbio-100814-125338>.
45. Harris, M.P. (2021). Bioelectric signaling as a unique regulator of development and regeneration. *Development* **148**, dev180794. <https://doi.org/10.1242/dev.180794>.
46. Adams, D.S., Uzel, S.G.M., Akagi, J., Wlodkowic, D., Andreeva, V., Yellick, P.C., Devitt-Lee, A., Pare, J.F., and Levin, M. (2016). Bioelectric signalling via potassium channels: a mechanism for craniofacial dysmorphogenesis in KCNJ2-associated Andersen-Tawil Syndrome. *J. Physiol.* **594**, 3245–3270. <https://doi.org/10.1113/JP271930>.
47. Vandenberg, L.N., Morrie, R.D., and Adams, D.S. (2011). V-ATPase-dependent ectodermal voltage and pH regionalization are required for craniofacial morphogenesis. *Dev. Dyn.* **240**, 1889–1904. <https://doi.org/10.1002/dvdy.22685>.
48. Beane, W.S., Morokuma, J., Adams, D.S., and Levin, M. (2011). Chemical genetics approach reveals H,K-ATPase-mediated membrane voltage is required for planarian head regeneration. *Chem. Biol.* **18**, 77–89. <https://doi.org/10.1016/j.chembiol.2010.11.012>.
49. Durant, F., Bischof, J., Fields, C., Morokuma, J., LaPalme, J., Hoi, A., and Levin, M. (2019). The Role of Early Bioelectric Signals in the Regeneration of Planarian Anterior/Posterior Polarity. *Biophys. J.* **116**, 948–961. <https://doi.org/10.1016/j.bpj.2019.01.029>.
50. Stern, C.D. (1982). Experimental reversal of polarity in chick embryo epiblast sheets in vitro. *Exp. Cell Res.* **140**, 468–471.
51. Levin, M., Thorlin, T., Robinson, K.R., Nogi, T., and Mercola, M. (2002). Asymmetries in H⁺/K⁺-ATPase and cell membrane potentials comprise a very early step in left-right patterning. *Cell* **111**, 77–89. [https://doi.org/10.1016/s0092-8674\(02\)00939-x](https://doi.org/10.1016/s0092-8674(02)00939-x).
52. Adams, D.S., Robinson, K.R., Fukumoto, T., Yuan, S., Albertson, R.C., Yellick, P., Kuo, L., McSweeney, M., and Levin, M. (2006). Early, H⁺-V-ATPase-dependent proton flux is necessary for consistent left-right patterning of non-mammalian vertebrates. *Development* **133**, 1657–1671. <https://doi.org/10.1242/dev.02341>.
53. Pai, V.P., Aw, S., Shomrat, T., Lemire, J.M., and Levin, M. (2012). Transmembrane voltage potential controls embryonic eye patterning in *Xenopus laevis*. *Development* **139**, 313–323. <https://doi.org/10.1242/dev.073759>.
54. Nuckles, R.J., Ng, A., Darland, T., and Gross, J.M. (2009). The vacuolar ATPase complex regulates retinoblast proliferation and survival, photo-
- receptor morphogenesis, and pigmentation in the zebrafish eye. *Investig. Ophthalmol. Vis. Sci.* **50**, 893–905.
55. Schotthofer, S.K., and Bohrman, J. (2020). Analysing bioelectrical phenomena in the *Drosophila* ovary with genetic tools: tissue-specific expression of sensors for membrane potential and intracellular pH, and RNAi-knockdown of mechanisms involved in ion exchange. *BMC Dev. Biol.* **20**, 15. <https://doi.org/10.1186/s12861-020-00220-6>.
56. Weiß, I., and Bohrman, J. (2019). Electrochemical gradients are involved in regulating cytoskeletal patterns during epithelial morphogenesis in the *Drosophila* ovary. *BMC Dev. Biol.* **19**, 22. <https://doi.org/10.1186/s12861-019-0203-y>.
57. Weiß, I., and Bohrman, J. (2019). Electrochemical patterns during *Drosophila* oogenesis: ion-transport mechanisms generate stage-specific gradients of pH and membrane potential in the follicle-cell epithelium. *BMC Dev. Biol.* **19**, 12. <https://doi.org/10.1186/s12861-019-0192-x>.
58. Woodruff, R.I., and Telfer, W.H. (1973). Polarized intercellular bridges in ovarian follicles of the cecropia moth. *J. Cell Biol.* **58**, 172–188.
59. Telfer, W.H., and Woodruff, R.I. (2002). Ion physiology of vitellogenic follicles. *J. Insect Physiol.* **48**, 915–923.
60. Jiang, T.-X., Li, A., Lin, C.M., Chiu, C., Cho, J.H., Reid, B., Zhao, M., Chow, R.H., Widelitz, R.B., and Chuong, C.M. (2021). Global feather orientations changed by electric current. *iScience* **24**, 102671. <https://doi.org/10.1016/j.isci.2021.102671>.
61. Silic, M.R., and Zhang, G. (2023). Bioelectricity in Developmental Patterning and Size Control: Evidence and Genetically Encoded Tools in the Zebrafish Model. *Cells* **12**, 1148. <https://doi.org/10.3390/cells12081148>.
62. Yi, C., Spitters, T.W., Al-Far, E.A.D.A., Wang, S., Xiong, T., Cai, S., Yan, X., Guan, K., Wagner, M., El-Armouche, A., and Antos, C.L. (2021). A calcineurin-mediated scaling mechanism that controls a K⁺-leak channel to regulate morphogen and growth factor transcription. *eLife* **10**, e60691. <https://doi.org/10.7554/eLife.60691>.
63. Kujawski, S., Lin, W., Kitte, F., Börmel, M., Fuchs, S., Arulmozhivarman, G., Vogt, S., Theil, D., Zhang, Y., and Antos, C.L. (2014). Calcineurin regulates coordinated outgrowth of zebrafish regenerating fins. *Dev. Cell* **28**, 573–587. <https://doi.org/10.1016/j.devcel.2014.01.019>.
64. Perathoner, S., Daane, J.M., Henrion, U., Seebohm, G., Higdon, C.W., Johnson, S.L., Nüsslein-Volhard, C., and Harris, M.P. (2014). Bioelectric signaling regulates size in zebrafish fins. *PLoS Genet.* **10**, e1004080. <https://doi.org/10.1371/journal.pgen.1004080>.
65. Belus, M.T., Rogers, M.A., Elzubeir, A., Josey, M., Rose, S., Andreeva, V., Yellick, P.C., and Bates, E.A. (2018). Kir2.1 is important for efficient BMP signaling in mammalian face development. *Dev. Biol.* **444**, S297–S307. <https://doi.org/10.1016/j.ydbio.2018.02.012>.
66. Pai, V.P., Martyniuk, C.J., Echeverri, K., Sundelacruz, S., Kaplan, D.L., and Levin, M. (2016). Genome-wide analysis reveals conserved transcriptional responses downstream of resting potential change in *Xenopus* embryos, axolotl regeneration, and human mesenchymal cell differentiation. *Regeneration* **3**, 3–25. <https://doi.org/10.1002/reg2.48>.
67. Chernet, B.T., and Levin, M. (2013). Transmembrane voltage potential is an essential cellular parameter for the detection and control of tumor development in a *Xenopus* model. *Dis. Model. Mech.* **6**, 595–607. <https://doi.org/10.1242/dmm.010835>.
68. Sundelacruz, S., Levin, M., and Kaplan, D.L. (2009). Role of membrane potential in the regulation of cell proliferation and differentiation. *Stem Cell Rev. Rep.* **5**, 231–246. <https://doi.org/10.1007/s12015-009-9080-2>.
69. Blackiston, D.J., McLaughlin, K.A., and Levin, M. (2009). Bioelectric controls of cell proliferation: ion channels, membrane voltage and the cell cycle. *Cell Cycle* **8**, 3527–3536. <https://doi.org/10.4161/cc.8.21.9888>.
70. Zhou, Y., Wong, C.O., Cho, K.J., van der Hoeven, D., Liang, H., Thakur, D.P., Luo, J., Babic, M., Zinsmaier, K.E., Zhu, M.X., et al. (2015). Membrane

- potential modulates plasma membrane phospholipid dynamics and K-Ras signaling. *Science* 349, 873–876.
71. Tseng, A., and Levin, M. (2013). Cracking the bioelectric code: Probing endogenous ionic controls of pattern formation. *Commun. Integr. Biol.* 6, e22595. <https://doi.org/10.4161/cib.22595>.
72. Tseng, A.S., Beane, W.S., Lemire, J.M., Masi, A., and Levin, M. (2010). Induction of vertebrate regeneration by a transient sodium current. *J. Neurosci.* 30, 13192–13200. <https://doi.org/10.1523/JNEUROSCI.3315-10.2010>.
73. Chernet, B.T., Adams, D.S., Lobikin, M., and Levin, M. (2016). Use of genetically encoded, light-gated ion translocators to control tumorigenesis. *Oncotarget* 7, 19575–19588. <https://doi.org/10.1863/oncotar.get.8036>.
74. Zhao, S., Mehta, A.S., and Zhao, M. (2020). Biomedical applications of electrical stimulation. *Cell. Mol. Life Sci.* 77, 2681–2699. <https://doi.org/10.1007/s00018-019-03446-1>.
75. Reid, B., and Zhao, M. (2014). The Electrical Response to Injury: Molecular Mechanisms and Wound Healing. *Adv. Wound Care* 3, 184–201. <https://doi.org/10.1089/wound.2013.0442>.
76. Zhao, M., Chalmers, L., Cao, L., Vieira, A.C., Mannis, M., and Reid, B. (2012). Electrical signaling in control of ocular cell behaviors. *Prog. Retin. Eye Res.* 31, 65–88. <https://doi.org/10.1016/j.preteyeres.2011.10.001>.
77. Balasubramanian, S., Weston, D.A., Levin, M., and Davidian, D.C.C. (2024). Electroceuticals: emerging applications beyond the nervous system and excitable tissues. *Trends Pharmacol. Sci.* 45, 391–394. <https://doi.org/10.1016/j.tips.2024.03.001>.
78. Sanjuan-Alberte, P., and Rawson, F.J. (2019). Engineering the spark into bioelectronic medicine. *Ther. Deliv.* 10, 139–142. <https://doi.org/10.4155/tde-2019-0008>.
79. Levin, M., Selberg, J., and Rolandi, M. (2019). Endogenous Bioelectronics in Development, Cancer, and Regeneration: Drugs and Bioelectronic Devices as Electroceuticals for Regenerative Medicine. *iScience* 22, 519–533. <https://doi.org/10.1016/j.isci.2019.11.023>.
80. Levin, M. (2013). Reprogramming cells and tissue patterning via bioelectrical pathways: molecular mechanisms and biomedical opportunities. *Wiley Interdiscip. Rev. Syst. Biol. Med.* 5, 657–676. <https://doi.org/10.1002/wsbm.1236>.
81. Levin, M. (2014). Endogenous bioelectrical networks store non-genetic patterning information during development and regeneration. *J. Physiol.* 592, 2295–2305. <https://doi.org/10.1113/jphysiol.2014.271940>.
82. Sullivan, K.G., Emmons-Bell, M., and Levin, M. (2016). Physiological inputs regulate species-specific anatomy during embryogenesis and regeneration. *Commun. Integr. Biol.* 9, e1192733. <https://doi.org/10.1080/19420889.2016.1192733>.
83. Emmons-Bell, M., Durant, F., Hammelman, J., Bessonov, N., Volpert, V., Morokuma, J., Pinet, K., Adams, D.S., Pietak, A., Lobo, D., and Levin, M. (2015). Gap Junctional Blockade Stochastically Induces Different Species-Specific Head Anatomies in Genetically Wild-Type *Girardia* dorotocephala Flatworms. *Int. J. Mol. Sci.* 16, 27865–27896. <https://doi.org/10.3390/ijms161126065>.
84. Pai, V.P., and Levin, M. (2022). HCN2 channel-induced rescue of brain, eye, heart and gut teratogenesis caused by nicotine, ethanol and aberrant notch signalling. *Wound Repair Regen.* 30, 681–706. <https://doi.org/10.1111/wrr.13032>.
85. Pai, V.P., Cervera, J., Mafe, S., Willocq, V., Lederer, E.K., and Levin, M. (2020). HCN2 Channel-Induced Rescue of Brain Teratogenesis via Local and Long-Range Bioelectric Repair. *Front. Cell. Neurosci.* 14, 136. <https://doi.org/10.3389/fncel.2020.00136>.
86. Pai, V.P., Pietak, A., Willocq, V., Ye, B., Shi, N.Q., and Levin, M. (2018). HCN2 Rescues brain defects by enforcing endogenous voltage pre-patterns. *Nat. Commun.* 9, 998. <https://doi.org/10.1038/s41467-018-0334-5>.
87. Tabibzadeh, S., and Brown, O.R. (2024). Trending toward gero-electroceuticals that target membrane potential for reprogramming aging and lifespan. *Aging and Cancer* 5, 3–13. <https://doi.org/10.1002/aac2.12070>.
88. Pio-Lopez, L., and Levin, M. (2023). Morphoceuticals: Perspectives for discovery of drugs targeting anatomical control mechanisms in regenerative medicine, cancer and aging. *Drug Discov. Today* 28, 103585. <https://doi.org/10.1016/j.drudis.2023.103585>.
89. Famm, K., Litt, B., Tracey, K.J., Boyden, E.S., and Slaoui, M. (2013). Drug discovery: a jump-start for electroceuticals. *Nature* 496, 159–161. <https://doi.org/10.1038/496159a>.
90. Pavlov, V.A., and Tracey, K.J. (2022). Bioelectronic medicine: Preclinical insights and clinical advances. *Neuron* 110, 3627–3644. <https://doi.org/10.1016/j.neuron.2022.09.003>.
91. Cohen, M.I., and Morrill, G.A. (1969). Electric Field in Amphibian Embryo and Its Possible Role in Morphogenesis. *Biophys. J.* 9, A187.
92. McCaig, C.D. (1986). Electric fields, contact guidance and the direction of nerve growth. *J. Embryol. Exp. Morphol.* 94, 245–255.
93. Borgens, R.B., and Shi, R. (1995). Uncoupling histogenesis from morphogenesis in the vertebrate embryo by collapse of the transneurial tube potential. *Dev. Dyn.* 203, 456–467.
94. Shi, R., and Borgens, R.B. (1995). Three-dimensional gradients of voltage during development of the nervous system as invisible coordinates for the establishment of embryonic pattern. *Dev. Dyn.* 202, 101–114.
95. Borgens, R.B. (1984). Are limb development and limb regeneration both initiated by an integumentary wounding? A hypothesis. *Differentiation*. 28, 87–93.
96. Nuccitelli, R. (1995). Endogenous Electric Fields Measured in Developing Embryos. In *Electromagnetic Fields*, 250, M. Blank, ed. (Adv. Chem), pp. 109–124.
97. Nuccitelli, R. (2003). A role for endogenous electric fields in wound healing. *Curr. Top. Dev. Biol.* 58, 1–26.
98. Robinson, K.R., and McCaig, C. (1980). Electrical fields, calcium gradients, and cell growth. *Ann. N. Y. Acad. Sci.* 339, 132–138.
99. Cone, C.D., and Tongier, M. (1971). Control of somatic cell mitosis by simulated changes in the transmembrane potential level. *Oncology* 25, 168–182.
100. Cone, C.D. (1971). Unified theory on the basic mechanism of normal mitotic control and oncogenesis. *J. Theor. Biol.* 30, 151–181.
101. Cone, C.D., Jr. (1970). Variation of the transmembrane potential level as a basic mechanism of mitosis control. *Oncology* 24, 438–470.
102. Levin, M., Pietak, A.M., and Bischof, J. (2019). Planarian regeneration as a model of anatomical homeostasis: Recent progress in biophysical and computational approaches. *Semin. Cell Dev. Biol.* 87, 125–144. <https://doi.org/10.1016/j.semcd.2018.04.003>.
103. Cervera, J., Pietak, A., Levin, M., and Mafe, S. (2018). Bioelectrical coupling in multicellular domains regulated by gap junctions: A conceptual approach. *Bioelectrochemistry* 123, 45–61. <https://doi.org/10.1016/j.bioelechem.2018.04.013>.
104. Pietak, A., and Levin, M. (2017). Bioelectric gene and reaction networks: computational modelling of genetic, biochemical and bioelectrical dynamics in pattern regulation. *J. R. Soc. Interface* 14, 20170425. <https://doi.org/10.1098/rsif.2017.0425>.
105. Pietak, A., and Levin, M. (2016). Exploring Instructive Physiological Signaling with the Bioelectric Tissue Simulation Engine (BETSE). *Front. Bioeng. Biotechnol.* 4, 55. <https://doi.org/10.3389/fbioe.2016.00055>.
106. Carvalho, J. (2023). A computational model of cell membrane bioelectric polarization and depolarization, connected with cell proliferation, in different tissue geometries. *J. Theor. Biol.* 557, 111338. <https://doi.org/10.1016/j.jtbi.2022.111338>.
107. Cervera, J., Ramirez, P., Levin, M., and Mafe, S. (2020). Community effects allow bioelectrical reprogramming of cell membrane potentials in

- multicellular aggregates: Model simulations. *Phys. Rev. E* 102, 052412. <https://doi.org/10.1103/PhysRevE.102.052412>.
108. Cervera, J., Mesequer, S., Levin, M., and Mafe, S. (2020). Bioelectrical model of head-tail patterning based on cell ion channels and intercellular gap junctions. *Bioelectrochemistry* 132, 107410. <https://doi.org/10.1016/j.bioelechem.2019.107410>.
109. Cervera, J., Levin, M., and Mafe, S. (2020). Bioelectrical Coupling of Single-Cell States in Multicellular Systems. *J. Phys. Chem. Lett.* 11, 3234–3241. <https://doi.org/10.1021/acs.jpclett.0c00641>.
110. Burr, H.S., and Northrop, F.S.C. (1935). The electro-dynamic theory of life. *Q. Rev. Biol.* 10, 322–333.
111. Burr, H.S. (1941). Field properties of the developing frog's egg. *Proc. Natl. Acad. Sci. USA* 27, 276–281.
112. Burr, H.S. (1941). Changes in the field properties of mice with transplanted tumors. *Yale J. Biol. Med.* 13, 783–788.
113. Burr, H.S., and Northrop, F.S. (1939). Evidence for the existence of an electro dynamic field in living organisms. *Proc. Natl. Acad. Sci. USA* 25, 284–288.
114. Burr, H.S. (1972). Blueprint for immortality; the electric patterns of life (N. Spearman).
115. Pinotsis, D.A., and Miller, E.K. (2023). In vivo ephaptic coupling allows memory network formation. *Cereb. Cortex* 33, 9877–9895. <https://doi.org/10.1093/cercor/bhad251>.
116. Pinotsis, D.A., Fridman, G., and Miller, E.K. (2023). Cytoelectric coupling: Electric fields sculpt neural activity and "tune" the brain's infrastructure. *Prog. Neurobiol.* 226, 102465. <https://doi.org/10.1016/j.pneurobio.2023.102465>.
117. Pinotsis, D.A., and Miller, E.K. (2022). Beyond dimension reduction: Stable electric fields emerge from and allow representational drift. *Neuroimage* 253, 119058. <https://doi.org/10.1016/j.neuroimage.2022.119058>.
118. Chiang, C.C., Shivacharan, R.S., Wei, X., Gonzalez-Reyes, L.E., and Durand, D.M. (2019). Slow periodic activity in the longitudinal hippocampal slice can self-propagate non-synaptically by a mechanism consistent with ephaptic coupling. *J. Physiol.* 597, 249–269. <https://doi.org/10.1113/JP276904>.
119. Qiu, C., Shivacharan, R.S., Zhang, M., and Durand, D.M. (2015). Can Neural Activity Propagate by Endogenous Electrical Field? *J. Neurosci.* 35, 15800–15811. <https://doi.org/10.1523/JNEUROSCI.1045-15.2015>.
120. Anastassiou, C.A., Perin, R., Markram, H., and Koch, C. (2011). Ephaptic coupling of cortical neurons. *Nat. Neurosci.* 14, 217–223. <https://doi.org/10.1038/nn.2727>.
121. Anastassiou, C.A., Montgomery, S.M., Barahona, M., Buzsáki, G., and Koch, C. (2010). The effect of spatially inhomogeneous extracellular electric fields on neurons. *J. Neurosci.* 30, 1925–1936. <https://doi.org/10.1523/JNEUROSCI.3635-09.2010>.
122. Kamermans, M., and Fahrenfort, I. (2004). Ephaptic interactions within a chemical synapse: hemichannel-mediated ephaptic inhibition in the retina. *Curr. Opin. Neurobiol.* 14, 531–541.
123. Jefferys, J.G. (1995). Nonsynaptic modulation of neuronal activity in the brain: electric currents and extracellular ions. *Physiol. Rev.* 75, 689–723.
124. Davis, Z.W., Busch, A., Steward, C., Muller, L., and Reynolds, J. (2024). Horizontal cortical connections shape intrinsic traveling waves into feature-selective motifs that regulate perceptual sensitivity. *Cell Rep.* 43, 114707.
125. Miller, E.K., Brincat, S.L., and Roy, J.E. (2024). Cognition is an emergent property. *Curr. Opin. Behav. Sci.* 57, 101388.
126. van Bree, S., Levenstein, D., Krause, M.R., Voytek, B., and Gao, R. (2024). Decoupling measurement and process: on the epiphenomenon debate surrounding brain oscillations and field potentials. Preprint at PsyArXiv. <https://doi.org/10.31234/osf.io/knjfw>.
127. Wolfram, S. (1984). Universality and complexity in cellular automata. *Phys. Nonlinear Phenom.* 10, 1–35.
128. Packard, N.H., and Wolfram, S. (1985). Two-dimensional cellular automata. *J. Stat. Phys.* 38, 901–946.
129. Manicka, S., and Levin, M. (2022). Minimal Developmental Computation: A Causal Network Approach to Understand Morphogenetic Pattern Formation. *Entropy* 24, 107. <https://doi.org/10.3390/e24010107>.
130. Turing, A.M. (1952). The Chemical Basis of Morphogenesis. *Philos. Trans. R. Soc. Lond. Ser. B Biol. Sci.* 237, 37–72.
131. Manicka, S., Pai, V.P., and Levin, M. (2023). Information integration during bioelectric regulation of morphogenesis of the embryonic frog brain. *iScience* 26, 108398. <https://doi.org/10.1016/j.isci.2023.108398>.
132. Werner, S., Stückemann, T., Beirán Amigo, M., Rink, J.C., Jülicher, F., and Friedrich, B.M. (2015). Scaling and regeneration of self-organized patterns. *Phys. Rev. Lett.* 114, 138101.
133. Scalise, D., and Schulman, R. (2014). Designing modular reaction-diffusion programs for complex pattern formation. *Technology* 02, 55–66. <https://doi.org/10.1142/s2339547814500071>.
134. Woolley, T.E., Krause, A.L., and Gaffney, E.A. (2021). Bespoke Turing Systems. *Bull. Math. Biol.* 83, 41. <https://doi.org/10.1007/s11538-021-00870-y>.
135. Hazan, H., and Levin, M. (2022). Exploring The Behavior of Bioelectric Circuits using Evolution Heuristic Search. *Bioelectricity* 4, 207–227.
136. Boutillon, A., Banavar, S.P., and Campàs, O. (2024). Conserved physical mechanisms of cell and tissue elongation. *Development* 151, dev202687.
137. Goldwyn, J.H., and Rinzel, J. (2016). Neuronal coupling by endogenous electric fields: cable theory and applications to coincidence detector neurons in the auditory brain stem. *J. Neurophysiol.* 115, 2033–2051. <https://doi.org/10.1152/jn.00780.2015>.
138. Shifman, A.R., and Lewis, J.E. (2019). Elfenn: a generalized platform for modeling ephaptic coupling in spiking neuron models. *Front. Neuroinform.* 13, 35.
139. Cunha, G.M., Corso, G., Miranda, J.G.V., and Dos Santos Lima, G.Z. (2022). Ephaptic entrainment in hybrid neuronal model. *Sci. Rep.* 12, 1629.
140. Ellingsrud, A.J., Solbrå, A., Einevoll, G.T., Halnes, G., and Rognes, M.E. (2020). Finite element simulation of ionic electrodiffusion in cellular geometries. *Front. Neuroinform.* 14, 11.
141. Cakan, C., and Obermayer, K. (2020). Biophysically grounded mean-field models of neural populations under electrical stimulation. *PLoS Comput. Biol.* 16, e1007822.
142. Chan, B.W.-C. (2019). Lenia: Biology of Artificial Life. *Complex Syst.* 28, 251–286. <https://doi.org/10.25088/ComplexSystems.28.3.251>.
143. Plantec, E., Hamon, G., Etcheverry, M., Oudeyer, P., Moulin-Frier, C., and Chan, B.W. (2023). Flow-Lenia: Towards open-ended evolution in cellular automata through mass conservation and parameter localization. In *Artificial Life Conference Proceedings* 35 (MIT Press One Rogers Street), p. 131.
144. Mordvintsev, A., Niklasson, E., and Randazzo, E. (2020). Growing Neural Cellular Automata. *Distill*.
145. Husbands, P., Smith, T., Jakobi, N., and O'Shea, M. (1998). Better living through chemistry: Evolving GasNets for robot control. *Connect. Sci.* 10, 185–210.
146. Pal, S., and Melnik, R. (2025). Nonlocal models in biology and life sciences: Sources, developments, and applications. *Phys. Life Rev.* 53, 24–75. <https://doi.org/10.1016/j.plrev.2025.02.005>.
147. Jewell, T.J., Krause, A.L., Maini, P.K., and Gaffney, E.A. (2023). Patterning of nonlocal transport models in biology: The impact of spatial dimension. *Math. Biosci.* 366, 109093. <https://doi.org/10.1016/j.mbs.2023.109093>.
148. Nuccitelli, R. (2003). Endogenous electric fields in embryos during development, regeneration and wound healing. *Radiat. Prot. Dosimetry* 106, 375–383.

149. Nuccitelli, R. (1992). Endogenous ionic currents and DC electric fields in multicellular animal tissues. *Bioelectromagnetics* 1, 147–157.
150. Ferreira, F., Moreira, S., Zhao, M., and Barriga, E.H. (2025). Stretch-induced endogenous electric fields drive directed collective cell migration in vivo. *Nat. Mater.* 24, 462–470. <https://doi.org/10.1038/s41563-024-02060-2>.
151. McCaig, C.D. (1988). Nerve guidance: A role for bio-electric fields? *Prog. Neurobiol.* 30, 449–468.
152. Zhao, M., Forrester, J.V., and McCaig, C.D. (1999). A small, physiological electric field orients cell division. *Proc. Natl. Acad. Sci. USA* 96, 4942–4946.
153. Frith, T.J.R., Briscoe, J., and Boezi, G.L.M. (2024). From signalling to form: the coordination of neural tube patterning. *Curr. Top. Dev. Biol.* 159, 168–231.
154. Mathews, J., and Levin, M. (2017). Gap junctional signaling in pattern regulation: Physiological network connectivity instructs growth and form. *Dev. Neurobiol.* 77, 643–673. <https://doi.org/10.1002/dneu.22405>.
155. Palacios-Prado, N., and Bukauskas, F.F. (2009). Heterotypic gap junction channels as voltage-sensitive valves for intercellular signaling. *Proc. Natl. Acad. Sci. USA* 106, 14855–14860. <https://doi.org/10.1073/pnas.0901923106>.
156. Houghton, F.D. (2005). Role of gap junctions during early embryo development. *Reproduction* 129, 129–135. <https://doi.org/10.1530/rep.1.00277>.
157. Cervera, J., Alcaraz, A., and Mafe, S. (2014). Membrane potential bistability in nonexcitable cells as described by inward and outward voltage-gated ion channels. *J. Phys. Chem. B* 118, 12444–12450. <https://doi.org/10.1021/jp508304h>.
158. Cervera, J., Meseguer, S., and Mafe, S. (2016). The interplay between genetic and bioelectrical signaling permits a spatial regionalisation of membrane potentials in model multicellular ensembles. *Sci. Rep.* 6, 35201. <https://doi.org/10.1038/srep35201>.
159. Cervera, J., Meseguer, S., and Mafe, S. (2018). Intercellular Connectivity and Multicellular Bioelectric Oscillations in Nonexcitable Cells: A Biophysical Model. *ACS Omega* 3, 13567–13575. <https://doi.org/10.1021/acsomega.8b01514>.
160. Cervera, J., Manzanares, J.A., and Mafe, S. (2018). Cell-cell bioelectrical interactions and local heterogeneities in genetic networks: a model for the stabilization of single-cell states and multicellular oscillations. *Phys. Chem. Chem. Phys.* 20, 9343–9354. <https://doi.org/10.1039/C8CP00648B>.
161. Manicka, S., and Levin, M. (2019). Modeling somatic computation with non-neural bioelectric networks. *Sci. Rep.* 9, 18612. <https://doi.org/10.1038/s41598-019-54859-8>.
162. Urone, P., and Hinrichs, R. (2016). College Physics (State University of New York).
163. England, S.J., and Robert, D. (2022). The ecology of electricity and electrotreception. *Biol. Rev.* 97, 383–413.
164. Funk, R.H.W., Monsees, T., and Ozkucur, N. (2009). Electromagnetic effects - From cell biology to medicine. *Prog. Histochem. Cytochem.* 43, 177–264. <https://doi.org/10.1016/j.proghi.2008.07.001>.
165. Nakajima, K.-i., Zhu, K., Sun, Y.H., Hegyi, B., Zeng, Q., Murphy, C.J., Small, J.V., Chen-Izu, Y., Izumiya, Y., Penninger, J.M., and Zhao, M. (2015). KCNJ15/Kir4.2 couples with polyamines to sense weak extracellular electric fields in galvanotaxis. *Nat. Commun.* 6, 8532.
166. Rems, L., Kasimova, M.A., Testa, I., and Delémotte, L. (2020). Pulsed electric fields can create pores in the voltage sensors of voltage-gated ion channels. *Biophys. J.* 119, 190–205.
167. Belfeldt, M., Rebl, H., Peters, K., Sridharan, K., Staehlke, S., and Nebe, J. B. (2023). Sensing of physical factors by cells: electric field, mechanical forces, physical plasma and light—importance for tissue regeneration. *Biomed. Mater. Devices* 1, 146–161.
168. Cortese, B., Palamà, I.E., D'Amone, S., and Gigli, G. (2014). Influence of electrotaxis on cell behaviour. *Integr. Biol.* 6, 817–830. <https://doi.org/10.1039/c4ib00142g>.
169. Kennard, A.S., and Theriot, J.A. (2020). Osmolarity-independent electrical cues guide rapid response to injury in zebrafish epidermis. *eLife* 9, e62386.
170. Lin, B.-j., Tsao, S.H., Chen, A., Hu, S.K., Chao, L., and Chao, P.H.G. (2017). Lipid rafts sense and direct electric field-induced migration. *Proc. Natl. Acad. Sci. USA* 114, 8568–8573.
171. Sun, Y., Do, H., Gao, J., Zhao, R., Zhao, M., and Mogilner, A. (2013). Keratocyte fragments and cells utilize competing pathways to move in opposite directions in an electric field. *Curr. Biol.* 23, 569–574.
172. Thrivikraman, G., Boda, S.K., and Basu, B. (2018). Unraveling the mechanistic effects of electric field stimulation towards directing stem cell fate and function: A tissue engineering perspective. *Biomaterials* 150, 60–86.
173. Yang, Q., Jiang, N., Xu, H., Zhang, Y., Xiong, C., and Huang, J. (2021). Integration of electrotaxis and durotaxis in cancer cells: Subtle nonlinear responses to electromechanical coupling cues. *Biosens. Bioelectron.* 186, 113289.
174. Tsai, H.-F., IJspeert, C., and Shen, A.Q. (2020). Voltage-gated ion channels mediate the electrotaxis of glioblastoma cells in a hybrid PMMA/PDMS microdevice. *APL Bioeng.* 4, 036102.
175. Kunche, S., Yan, H., Calof, A.L., Lowengrub, J.S., and Lander, A.D. (2016). Feedback, Lineages and Self-Organizing Morphogenesis. *PLoS Comput. Biol.* 12, e1004814. <https://doi.org/10.1371/journal.pcbi.1004814>.
176. Perrimon, N., and McMahon, A.P. (1999). Negative feedback mechanisms and their roles during pattern formation. *Cell* 97, 13–16.
177. Wolpert, L. (1969). Positional information and the spatial pattern of cellular differentiation. *J. Theor. Biol.* 25, 1–47.
178. Levin, M. (2012). Morphogenetic fields in embryogenesis, regeneration, and cancer: non-local control of complex patterning. *Biosystems* 109, 243–261. <https://doi.org/10.1016/j.biosystems.2012.04.005>.
179. Petkova, M.D., Tkacik, G., Bialek, W., Wieschaus, E.F., and Gregor, T. (2019). Optimal Decoding of Cellular Identities in a Genetic Network. *Cell* 176, 844–855.e5. <https://doi.org/10.1016/j.cell.2019.01.007>.
180. Tononi, G., Sporns, O., and Edelman, G.M. (1994). A measure for brain complexity: relating functional segregation and integration in the nervous system. *Proc. Natl. Acad. Sci. USA* 91, 5033–5037.
181. Francis, J.T., Gluckman, B.J., and Schiff, S.J. (2003). Sensitivity of neurons to weak electric fields. *J. Neurosci.* 23, 7255–7261.
182. Weaver, J.C., Vaughan, T.E., Adair, R.K., and Astumian, R.D. (1998). Theoretical limits on the threshold for the response of long cells to weak extremely low frequency electric fields due to ionic and molecular flux rectification. *Biophys. J.* 75, 2251–2254.
183. Kelso, J.S. (1997). Dynamic Patterns: The Self-Organization of Brain and Behavior (MIT Press).
184. Manicka, S., and Levin, M. (2019). The Cognitive Lens: a primer on conceptual tools for analysing information processing in developmental and regenerative morphogenesis. *Philos. Trans. R. Soc. Lond. B Biol. Sci.* 374, 20180369. <https://doi.org/10.1098/rstb.2018.0369>.
185. McMillen, P., Oudin, M.J., Levin, M., and Payne, S.L. (2021). Beyond neurons: long distance communication in development and cancer. *Front. Cell Dev. Biol.* 9, 739024.
186. Berleth, T., and Sachs, T. (2001). Plant morphogenesis: long-distance coordination and local patterning. *Curr. Opin. Plant Biol.* 4, 57–62.
187. McMillen, P., Oudin, M.J., Levin, M., and Payne, S.L. (2021). Beyond Neurons: Long Distance Communication in Development and Cancer. *Front. Cell Dev. Biol.* 9, 739024. <https://doi.org/10.3389/fcell.2021.739024>.

188. Caviglia, S., and Ober, E.A. (2018). Non-conventional protrusions: the diversity of cell interactions at short and long distance. *Curr. Opin. Cell Biol.* 54, 106–113.
189. Hans, J. (2001). *Cymatics: A Study of Wave Phenomena and Vibration* (MACROmedia Publishing).
190. Hasegawa, Y. (2023). Unifying speed limit, thermodynamic uncertainty relation and Heisenberg principle via bulk-boundary correspondence. *Nat. Commun.* 14, 2828.
191. Amari, S.-i (1993). Backpropagation and stochastic gradient descent method. *Neurocomputing* 5, 185–196.
192. Burr, H.S. (1947). Field theory in biology. *Sci. Mon.* 64, 217–225.
193. Margenau, H. (1947). Particle and field concepts in biology. *Sci. Mon.* 64, 225–231.
194. Bischof, M. (1998). Holism and Field Theories in Biology. In *Biophotons*, J.J. Chang, J. Fisch, and F.A. Popp, eds. (Springer).
195. Tzambazakis, A. (2015). The evolution of the biological field concept. *Fields of the Cell*, 1–27 (Research Signpost).
196. Haraway, D.J. (1976). *Crystals, Fabrics and Fields- Metaphors of Organicism in Twentieth-Century Developmental Biology* (Yale University Press).
197. Levin, M. (2020). Revisiting Burr and Northrop's "The Electro-Dynamic Theory of Life" (1935). *Biol. Theory* 15, 83–90. <https://doi.org/10.1007/s13752-020-00341-y>.
198. Vittadello, S.T., Leyshon, T., Schnoerr, D., and Stumpf, M.P.H. (2021). Turing pattern design principles and their robustness. *Philos. Trans. A Math. Phys. Eng. Sci.* 379, 20200272. <https://doi.org/10.1098/rsta.2020.0272>.
199. Leyshon, T., Tonello, E., Schnoerr, D., Siebert, H., and Stumpf, M.P.H. (2021). The design principles of discrete turing patterning systems. *J. Theor. Biol.* 531, 110901. <https://doi.org/10.1016/j.jtbi.2021.110901>.
200. Schiffmann, Y. (2011). Turing-Child field underlies spatial periodicity in *Drosophila* and planarians. *Prog. Biophys. Mol. Biol.* 105, 258–269. <https://doi.org/10.1016/j.pbiomolbio.2010.12.007>.
201. Schiffmann, Y. (2008). The Turing-Child energy field as a driver of early mammalian development. *Prog. Biophys. Mol. Biol.* 98, 107–117. <https://doi.org/10.1016/j.pbiomolbio.2008.07.001>.
202. Steyn-Ross, M.L., Steyn-Ross, D.A., Wilson, M.T., and Sleigh, J.W. (2007). Gap junctions mediate large-scale Turing structures in a mean-field cortex driven by subcortical noise. *Phys. Rev. E Stat. Nonlin. Soft Matter Phys.* 76, 011916.
203. Schiffmann, Y. (1991). An hypothesis: phosphorylation fields as the source of positional information and cell differentiation-(cAMP, ATP) as the universal morphogenetic Turing couple. *Prog. Biophys. Mol. Biol.* 56, 79–105.
204. Green, J.B.A., and Sharpe, J. (2015). Positional information and reaction-diffusion: two big ideas in developmental biology combine. *Development* 142, 1203–1211. <https://doi.org/10.1242/dev.114991>.
205. Cooke, J., and Zeeman, E.C. (1976). A Clock and Wavefront Model for Control of the Number of Repeated Structures during Animal Morphogenesis. *J. Theor. Biol.* 58, 455–476.
206. Meinhardt, H. (1992). Pattern formation in biology: a comparison of models and experiments. *Rep. Prog. Phys.* 55, 797–849.
207. Fukumoto, T., Kema, I.P., and Levin, M. (2005). Serotonin signaling is a very early step in patterning of the left-right axis in chick and frog embryos. *Curr. Biol.* 15, 794–803. <https://doi.org/10.1016/j.cub.2005.03.044>.
208. Fukumoto, T., Blakely, R., and Levin, M. (2005). Serotonin transporter function is an early step in left-right patterning in chick and frog embryos. *Dev. Neurosci.* 27, 349–363. <https://doi.org/10.1159/000088451>.
209. Esser, A.T., Smith, K.C., Weaver, J.C., and Levin, M. (2006). Mathematical model of morphogen electrophoresis through gap junctions. *Dev. Dyn.* 235, 2144–2159. <https://doi.org/10.1002/dvdy.20870>.
210. Levin, M. (2014). Molecular bioelectricity: how endogenous voltage potentials control cell behavior and instruct pattern regulation in vivo. *Mol. Biol. Cell* 25, 3835–3850. <https://doi.org/10.1091/mbc.E13-12-0708>.
211. Ya-Feng, H., Fu-Cheng, L., Wei-Li, F., and Li-Fang, D. (2012). Controlling the transition between Turing and antipodal patterns by using time-delayed-feedback. *Chinese Phys. B* 21, 304–309.
212. Dúzs, B., Holló, G., Kitahata, H., Ginder, E., Suematsu, N.J., Lagzi, I., and Szalai, I. (2023). Appearance and suppression of Turing patterns under a periodically forced feed. *Commun. Chem.* 6, 3.
213. Marques-Pita, M., and Rocha, L.M. (2013). Canalization and control in automata networks: body segmentation in *Drosophila melanogaster*. *PLoS One* 8, e55946. <https://doi.org/10.1371/journal.pone.0055946>.
214. Gates, A.J., and Rocha, L.M. (2016). Control of complex networks requires both structure and dynamics. *Sci. Rep.* 6, 24456.
215. Herrera-Rincon, C., Golding, A.S., Moran, K.M., Harrison, C., Martyniuk, C.J., Guay, J.A., Zaltsman, J., Carabello, H., Kaplan, D.L., and Levin, M. (2018). Brief Local Application of Progesterone via a Wearable Bioreactor Induces Long-Term Regenerative Response in Adult *Xenopus* Hindlimb. *Cell Rep.* 25, 1593–1609.e7. <https://doi.org/10.1016/j.celrep.2018.10.010>.
216. Kim, D.H., Viventi, J., Amsden, J.J., Xiao, J., Vigeland, L., Kim, Y.S., Blanco, J.A., Panilaitis, B., Frechette, E.S., Contreras, D., et al. (2010). Dissolvable films of silk fibroin for ultrathin conformal bio-integrated electronics. *Nat. Mater.* 9, 511–517. <https://doi.org/10.1038/nmat2745>.
217. Cuttaz, E.A., Bailey, Z.K., Chapman, C.A.R., Goding, J.A., and Green, R. A. (2024). Polymer Bioelectronics: A Solution for Both Stimulating and Recording Electrodes. *Adv. Healthc. Mater.* 13, e2304447. <https://doi.org/10.1002/adhm.202304447>.
218. Euler, L., Juthberg, R., Flodin, J., Guo, L., Ackermann, P.W., and Person, N.K. (2021). Textile Electrodes: Influence of Electrode Construction and Pressure on Stimulation Performance in Neuromuscular Electrical Stimulation (NMES). *Annu. Int. Conf. IEEE Eng. Med. Biol. Soc.* 2021, 1305–1308. <https://doi.org/10.1109/EMBC46164.2021.9630649>.
219. Anastassiou, C.A., and Koch, C. (2015). Ephaptic coupling to endogenous electric field activity: why bother? *Curr. Opin. Neurobiol.* 31, 95–103. <https://doi.org/10.1016/j.conb.2014.09.002>.
220. Weiss, S.A., and Faber, D.S. (2010). Field effects in the CNS play functional roles. *Front. Neural Circuits* 4, 15. <https://doi.org/10.3389/fncir.2010.00015>.
221. Ruffini, G., Salvador, R., Tadayon, E., Sanchez-Todo, R., Pascual-Leone, A., and Santaronecchi, E. (2020). Realistic modeling of mesoscopic ephaptic coupling in the human brain. *PLoS Comput. Biol.* 16, e1007923.
222. Hesp, C. (2021). Beyond connectionism: A neuronal dance of ephaptic and synaptic interactions: Commentary on "The growth of cognition: Free energy minimization and the embryogenesis of cortical computation" by Wright and Bourke (2020). *Phys. Life Rev.* 36, 40–43. <https://doi.org/10.1016/j.plrev.2020.08.002>.
223. Busse, S.M., McMillen, P.T., and Levin, M. (2018). Cross-limb communication during *Xenopus* hindlimb regenerative response: non-local bioelectric injury signals. *Development* 145, dev164210. <https://doi.org/10.1242/dev.164210>.
224. Kornberg, T.B., and Roy, S. (2014). Communicating by touch-neurons are not alone. *Trends Cell Biol.* 24, 370–376. <https://doi.org/10.1016/j.tcb.2014.01.003>.
225. Turing, A.M. (1990). The chemical basis of morphogenesis. *Bull. Math. Biol.* 52, 153.
226. Hartl, B., Risi, S., and Levin, M. (2024). Evolutionary Implications of Self-Assembling Cybernetic Materials with Collective Problem-Solving Intelligence at Multiple Scales. *Entropy* 26, 532. <https://doi.org/10.3390/e26070532>.
227. Stramer, B.M. (2024). The extracellular matrix in tissue morphogenesis: No longer a backseat driver. *Cells Dev.* 177, 203883.

228. Pauly, H., and Schwan, H.P. (1966). Dielectric properties and ion mobility in erythrocytes. *Biophys. J.* 6, 621–639.
229. Asami, K., Takahashi, Y., and Takashima, S. (1989). Dielectric properties of mouse lymphocytes and erythrocytes. *Biochim. Biophys. Acta 1010*, 49–55.
230. Andreev, V.P. (2013). Cytoplasmic electric fields and electroosmosis: possible solution for the paradoxes of the intracellular transport of biomolecules. *PLoS One* 8, e61884.
231. Asami, K., and Irimajiri, A. (2000). Dielectrospectroscopic monitoring of early embryogenesis in single frog embryos. *Phys. Med. Biol.* 45, 3285–3297.
232. Das, D., Kamil, F.A., Biswas, K., and Das, S. (2014). Evaluation of single cell electrical parameters from bioimpedance of a cell suspension. *RSC Adv.* 4, 18178–18185.
233. Nasir, N., and Al Ahmad, M. (2020). Cells electrical characterization: dielectric properties, mixture, and modeling theories. *J. Eng.* 2020, 1–17.
234. Pai, V.P., Zhang, G., and Levin, M. (2024). “Bioelectricity in Development, Regeneration, and Cancers” *Cell Bio 2023: A Joint Meeting of the American Society of Cell Biology and European Molecular Biology Organization December 2–6, 2023, in Boston, MA, USA. Bioelectricity* 6, 65–68.
235. Pai, V.P., Lemire, J.M., Paré, J.F., Lin, G., Chen, Y., and Levin, M. (2015). Endogenous Gradients of Resting Potential Instructively Pattern Embryonic Neural Tissue via Notch Signaling and Regulation of Proliferation. *J. Neurosci.* 35, 4366–4385. <https://doi.org/10.1523/JNEUROSCI.1877-14.2015>.
236. Pai, V.P., Lemire, J.M., Chen, Y., Lin, G., and Levin, M. (2015). Local and long-range endogenous resting potential gradients antagonistically regulate apoptosis and proliferation in the embryonic CNS. *Int. J. Dev. Biol.* 59, 327–340. <https://doi.org/10.1387/ijdb.150197ml>.
237. Gunawardena, J. (2014). Models in biology: ‘accurate descriptions of our pathetic thinking. *BMC Biol.* 12, 29.
238. Lobo, D., Solano, M., Bubenik, G.A., and Levin, M. (2014). A linear-en-coding model explains the variability of the target morphology in regeneration. *J. R. Soc. Interface* 11, 20130918. <https://doi.org/10.1098/rsif.2013.0918>.
239. Mordvintsev, A., Olah, C., and Tyka, M. (2015). Deepdream-a code example for visualizing neural networks. *Google Research* 2, 67.
240. Hechavarria, D., Dewilde, A., Braunhut, S., Levin, M., and Kaplan, D.L. (2010). BioDome regenerative sleeve for biochemical and biophysical stimulation of tissue regeneration. *Med. Eng. Phys.* 32, 1065–1073. <https://doi.org/10.1016/j.medengphy.2010.07.010>.
241. Murugan, N.J., Vigran, H.J., Miller, K.A., Golding, A., Pham, Q.L., Sperry, M.M., Rasmussen-Ivey, C., Kane, A.W., Kaplan, D.L., and Levin, M. (2022). Acute multidrug delivery via a wearable bioreactor facilitates long-term limb regeneration and functional recovery in adult *Xenopus laevis*. *Sci. Adv.* 8, eabj2164. <https://doi.org/10.1126/sciadv.abj2164>.
242. Ebrahimkhani, M.R., and Levin, M. (2021). Synthetic living machines: A new window on life. *iScience* 24, 102505. <https://doi.org/10.1016/j.isci.2021.102505>.
243. Velazquez, J.J., Su, E., Cahan, P., and Ebrahimkhani, M.R. (2018). Programming Morphogenesis through Systems and Synthetic Biology. *Trends Biotechnol.* 36, 415–429. <https://doi.org/10.1016/j.tibtech.2017.11.003>.
244. Kamm, R.D., Bashir, R., Arora, N., Dar, R.D., Gillette, M.U., Griffith, L.G., Kemp, M.L., Kinlaw, K., Levin, M., Martin, A.C., et al. (2018). Perspective: The promise of multi-cellular engineered living systems. *APL Bioeng.* 2, 040901. <https://doi.org/10.1063/1.5038337>.
245. Teague, B.P., Guye, P., and Weiss, R. (2016). Synthetic Morphogenesis. *Cold Spring Harb. Perspect. Biol.* 8, a023929. <https://doi.org/10.1101/cshperspect.a023929>.
246. Cover, T.M. (1999). *Elements of Information Theory* (John Wiley & Sons).
247. James, R.G., Ellison, C.J., and Crutchfield, J.P. (2018). “dit”: a Python package for discrete information theory. *J. Open Source Softw.* 3, 738.
248. Riedmiller, M., and Braun, H. (1992). RPROP-A fast adaptive learning algorithm. In Proc of ISCIS VII, Universitat (Citeseer).
249. Paszke, A., Gross, S., Massa, F., Lerer, A., Bradbury, J., Chanan, G., Killen, T., Lin, Z., Gimelshein, N., Antiga, L., et al. (2019). Pytorch: An imperative style, high-performance deep learning library. *Adv. Neural Inf. Process. Syst.* 32, 8026–8037.

Supplemental information

**Field-mediated bioelectric basis
of morphogenetic prepatternning**

Santosh Manicka and Michael Levin

Supplemental Information

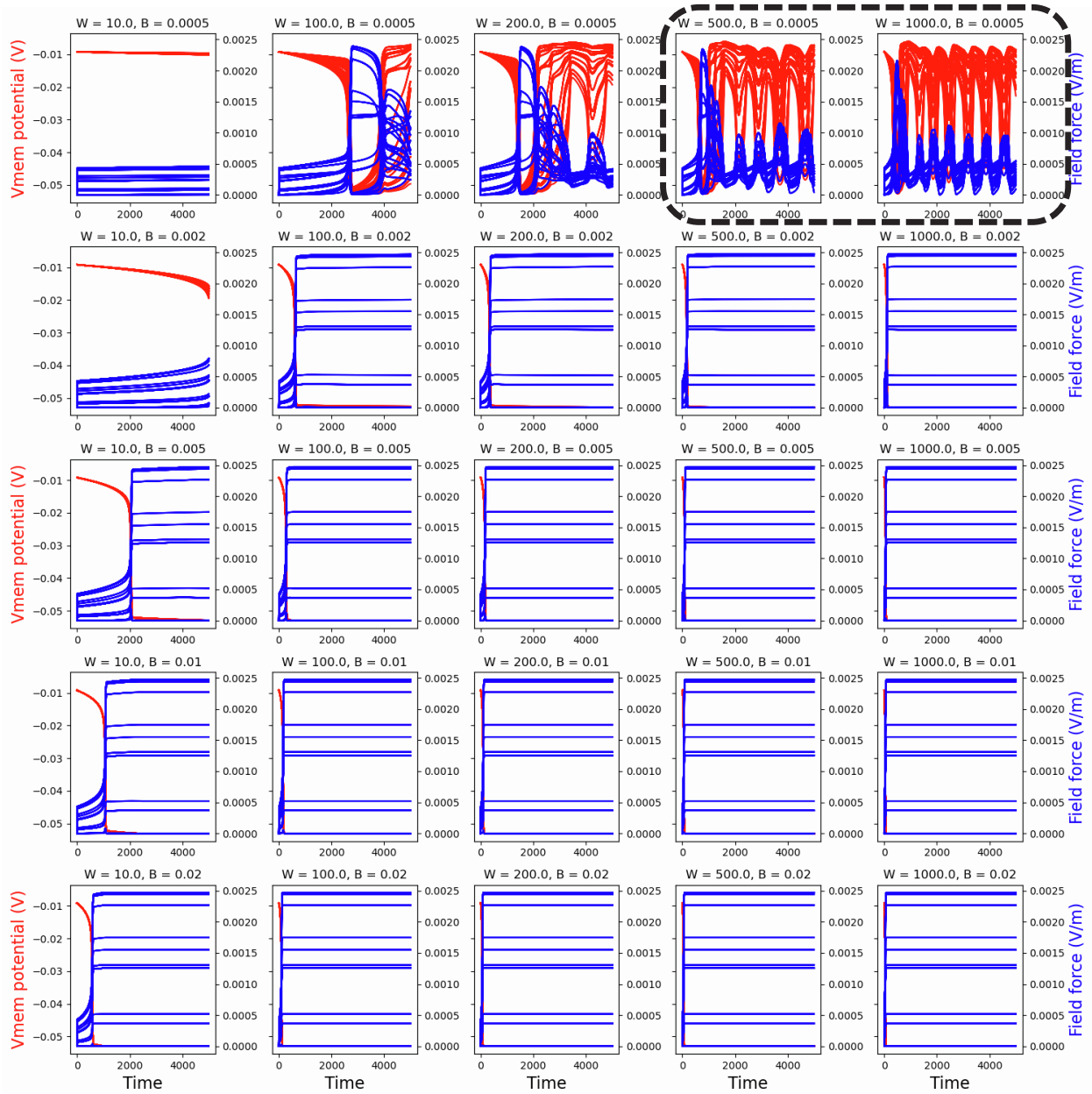


Figure S1. Behavior of the model with a relatively short field range and strong gap junctional strength. (Individual panels) Timeseries of V_{mem} (red) and field force magnitudes (blue) for models with various combinations of W and B , and $R=4$ and $G=1.0$. Highlighted in a dashed box are the subsets that depict the slowest variation of the field compared to V_{mem} . These are the same subsets that correspond with maximization of various dynamical properties (Figures 4-6) for $R=4$. Note that even though V_{mem} is expressed in volts it is in reality expressed as a potential difference between the center and the exterior of the cell (effectively equal to the cell's radius equal to 5×10^{-6} m); therefore, the numbers stated in the V_{mem} axis should be multiplied by 10^6 when expressed in units of V/m.

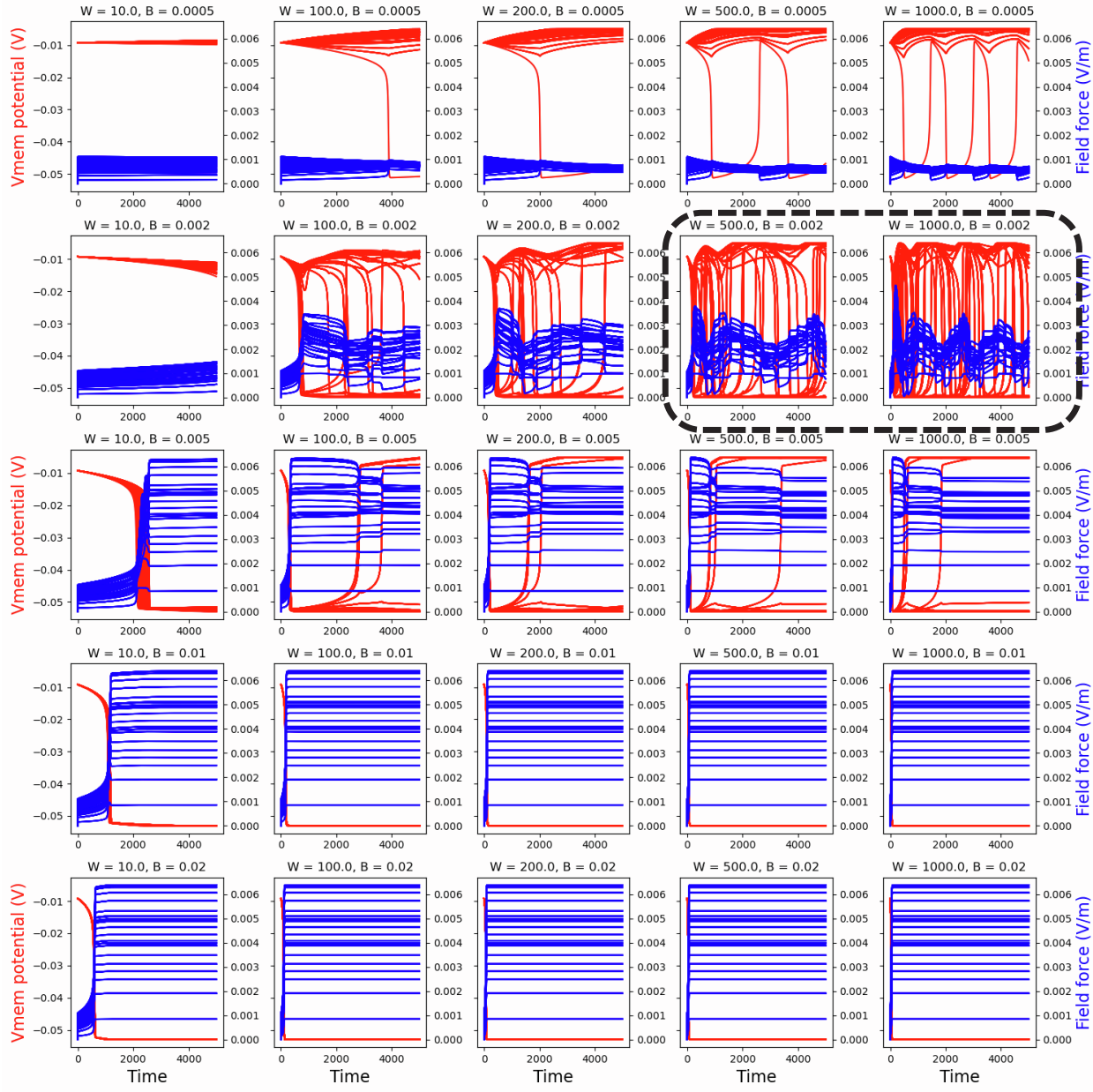


Figure S2. Behavior of the model with an intermediate field range and weak gap junctional strength. (Individual panels) Timeseries of V_{mem} (red) and field force magnitudes (blue) for models with various combinations of W and B , and $R=10$ and $G=0.05$. Highlighted in a dashed box are the subsets that depict the slowest variation of the field compared to V_{mem} . These are the same subsets that correspond with maximization of various dynamical properties (Figures 4-6) for $R=10$. Note that even though V_{mem} is expressed in volts it is in reality expressed as a potential difference between the center and the exterior of the cell (effectively equal to the cell's radius equal to 5×10^{-6} m); therefore, the numbers stated in the V_{mem} axis should be multiplied by 10^6 when expressed in units of V/m.

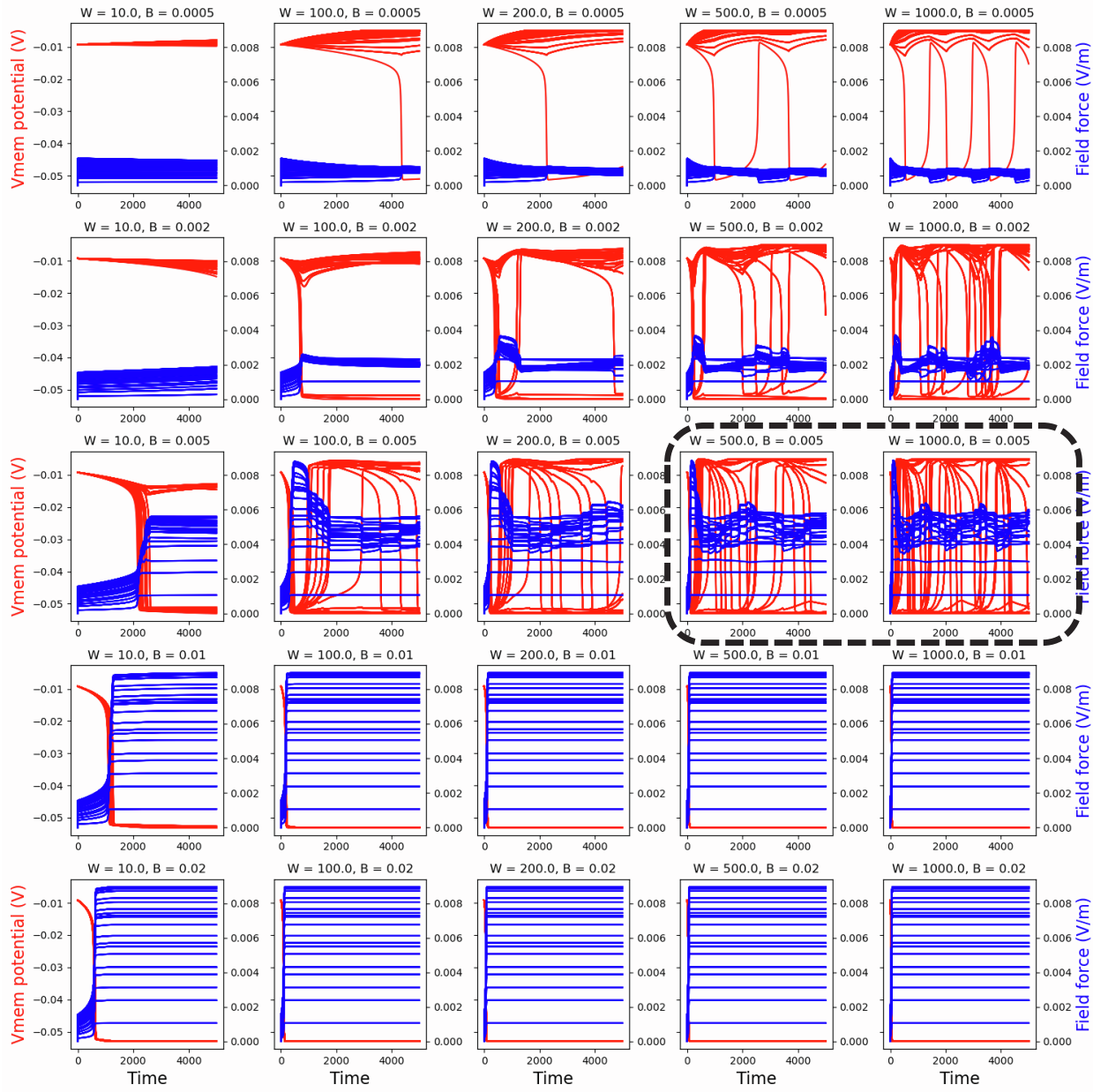


Figure S3. Behavior of the model with a long field range and weak gap junctional strength. (Individual panels) Timeseries of V_{mem} (red) and field force magnitudes (blue) for models with various combinations of W and B , and $R=21$ and $G=0.05$. Highlighted in a dashed box are the subsets that depict the slowest variation of the field compared to V_{mem} . These are the same subsets that correspond with maximization of various dynamical properties (Figures 4-6) for $R=21$. Note that even though V_{mem} is expressed in volts it is in reality expressed as a potential difference between the center and the exterior of the cell (effectively equal to the cell's radius equal to 5×10^{-6} m); therefore, the numbers stated in the V_{mem} axis should be multiplied by 10^6 when expressed in units of V/m.

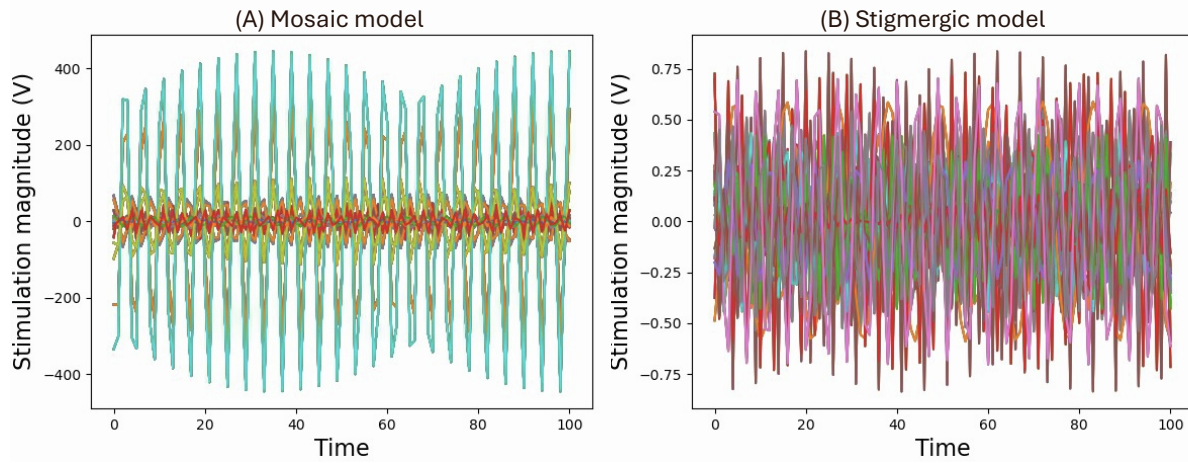


Figure S4. Profiles of the exogenous stimulation applied to the vertebrate face patterning models. (A) Timeseries of the oscillatory stimulation applied to the boundaries of the mosaic model during the initial 10% (equal to 100 steps) of the simulation phase, and (B) equivalently for the stigmergic model. The total number of traces in each panel is 44, indicating the total number of field grid points at the boundary of the 11x11 tissue with a 12x12 layout of the field grid points. Due to the bilateral symmetry of the smiley pattern, the total number of distinct traces is only 22, corresponding to one vertical half of the boundary, with the other being its mirror reflection.

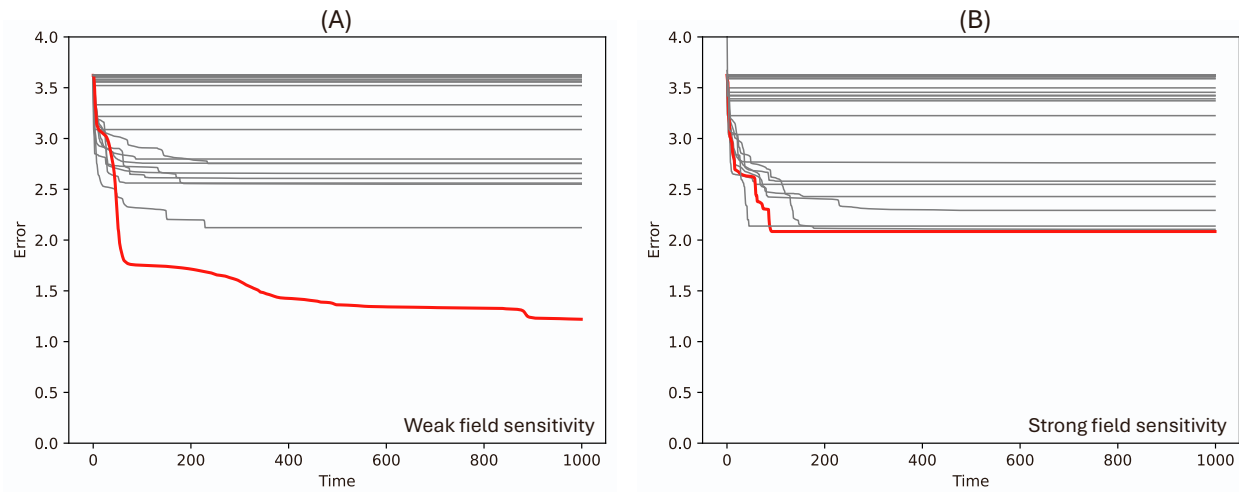


Figure S5. Optimization trends of the vertebrate face patterning models. (A) Time-evolution of the losses (errors computed as the Euclidean distance between the observed V_{mem} pattern and a target face pattern) of a population of 100 models each in model class with weak field sensitivity, and (B) equivalently for models with strong field sensitivity. Red lines in each class indicate the models with the lowest asymptotic error in the respective class and chosen for further analysis in the main paper (mosaic and stigmergic models respectively).

| | Stigmergic model | Mosaic model |
|--|--------------------|---------------|
| $\widehat{MI}(\text{Boundary}; \text{Bulk})$ | 0.7 ± 0.0 | 0.2 ± 0.0 |
| $\widehat{CS}(\text{Boundary}, \text{Bulk})$ | 0.8 ± 0.0 | 0.5 ± 0.0 |
| ΔD | $44.5\% \pm 0.8\%$ | 0% |
| RFC | 6.6% | 2.5% |

Table S1. Stigmergic model displays greater bulk-boundary interactions than the mosaic model. Table shows the metrics of boundary-bulk mutual information (\widehat{MI}), causal strength of directed interactions flowing from boundary to bulk (\widehat{CS}), degree of deformity in the pattern caused due to permutation of the boundary states (ΔD) and RFC, present in the respective models. The numbers, including the standard deviations, have been rounded to one significant digit.

Video S1. Animation of the V_{mem} pattern and the electric force field profile for a model with parameters $R=4$, $G=0.05$, $W=1000$, $B=0.0005$. Model was run for 5000 steps (movie sampled with every twentieth frame with a frame rate of 10 fps). Video available at <https://youtu.be/LRmgqd1Tu64>

Video S2. Animation of the V_{mem} pattern and the electric force field profile for a model with parameters $R=10$, $G=0.05$, $W=1000$, $B=0.002$. Model was run for 5000 steps (movie sampled with every twentieth frame with a frame rate of 10 fps). Video available at <https://youtu.be/bpa56ySJSXl>

Video S3. Animation of the V_{mem} pattern and the electric force field profile for a model with parameters $R=21$, $G=0.05$, $W=1000$, $B=0.005$. Model was run for 5000 steps (movie sampled with every twentieth frame with a frame rate of 10 fps). Video available at <https://youtu.be/kmmeUY2nqRg>